Received: 28 March 2018 | Revised: 15 August 2018 | Accepted: 14 November 2018 | Published on: 7 April 2019

DOI: 10.1002/qj.3439

INCOMPASS SPECIAL COLLECTION

Quarterly Journal of the Royal Meteorological Society RMetS

The dynamic and thermodynamic structure of the monsoon over southern India: New observations from the INCOMPASS IOP

Jennifer K. Fletcher[1] | Douglas J. Parker[1] | Andrew G. Turner[2,3] | Arathy Menon[2,3] | Gill M. Martin[4] | Cathryn E. Birch[1] | Ashis K. Mitra[5] | G. Mrudula[6] | Kieran M. R. Hunt[2] | Christopher M. Taylor[7,8] | Robert A. Houze[9,10] | Stella R. Brodzik[8] | G. S. Bhat[11]

[1]School of Earth and Environment, University of Leeds, Leeds, UK
[2]Department of Meteorology, University of Reading, Reading, UK
[3]National Centre for Atmospheric Science, University of Reading, Reading, UK
[4]Met Office Hadley Centre, Exeter, UK
[5]National Centre for Medium Range Weather Forecasting, Noida, India
[6]CSIR–National Aerospace Laboratories, Bengaluru, India
[7]Centre for Ecology and Hydrology, Wallingford, UK
[8]National Centre for Earth Observation, Wallingford, UK
[9]Department of Atmospheric Sciences, University of Washington, Seattle, WA, USA
[10]Pacific Northwest National Laboratory, Richland, SC, USA
[11]Centre for Atmospheric and Oceanic Sciences, Indian Institute of Science, Bengaluru, India

Correspondence
Jennifer K. Fletcher, School of Earth and Environment, University of Leeds, Leeds LS2 9JT, UK.
Email: j.k.fletcher@leeds.ac.uk

Funding information
NERC grants NE/L013843/1, NE/L01386X/1 and NE/L013819, a Royal Society Wolfson Research Merit Award, the Indian Ministry of Earth Sciences through its Monsoon Mission Program, the Joint UK BEIS/Defra Met Office Hadley Centre Climate Programme (GA01101), National Science Foundation grants AGS-1503155 and AGS-1503155, NASA grants NNX16AD75G and NNX16AD75G, and the Pacific Northwest National Laboratory under task order 292896 (WACCEM) of master agreement 243766.

Some of the highest summer monsoon rainfall in South Asia falls on the windward slopes of the Western Ghats mountains on India's west coast and offshore over the eastern Arabian Sea. Understanding of the processes determining the spatial distribution and temporal variability of this region remains incomplete. In this paper, new Interaction of Convective Organization and Monsoon Precipitation, Atmosphere, Surface and Sea (INCOMPASS) aircraft and ground-based measurements of the summer monsoon over the Western Ghats and upstream of them are presented and placed within the context of remote-sensing observations and reanalysis. The transition from widespread rainfall over the eastern Arabian Sea to rainfall over the Western Ghats is documented in high spatial and temporal resolution. Heavy rainfall offshore during the campaign was associated primarily with mid-tropospheric humidity, secondarily with sea surface temperature, and only weakly with orographic blocking. A mid-tropospheric dry intrusion suppressed deep convection offshore in the latter half of the campaign, allowing the build-up of low-level humidity in the onshore flow and enhancing rainfall over the mountains. Rainfall on the lee side of the Western Ghats occurred during the latter half of the campaign in association with enhanced mesoscale easterly upslope flow. Diurnal cycles in rainfall offshore (maximum in the morning) and on the mountains (maximum in the afternoon) were observed. Considerable zonal and temporal variability was seen in the offshore boundary layer, suggesting the presence of convective downdraughts and cold pools. Persistent drying of the subcloud mixed layer several hundred kilometres off the coast was observed, suggesting strong mixing between the boundary layer and the free troposphere. These observations provide quantitative targets to test models and suggest hypotheses on the physical mechanisms determining the distribution and variability in rainfall in the Western Ghats region.

KEYWORDS
field campaigns, INCOMPASS, Indian monsoon

1 | INTRODUCTION

The summertime South Asian monsoon (June–September, hereafter referred to as the monsoon) is well known for abrupt and dramatic changes it brings to Indian rainfall. There is considerable spatial variability in the monsoon rainfall, much of it associated with topography and gradients in sea surface temperature (SST). Over southern India, the monsoon is characterized by zonal contrasts in both rainfall and surface conditions between the Arabian Sea, the west coast of peninsular India, and the Bay of Bengal. The western Arabian Sea surface is relatively cool due to coastal upwelling (Saha, 1970) associated with the southwesterly monsoon flow. SST is higher in the eastern Arabian Sea (Shukla, 1975; McCreary and Kundu, 1989) and higher still in the Bay of Bengal (Bhat *et al.*, 2004). The free troposphere over the Arabian Sea is much drier than over the Bay of Bengal, and over the western Arabian Sea an inversion caps convection, which transitions from shallow to deep from the western to eastern Arabian Sea (Sathiyamoorthy *et al.*, 2013). Both SST and thermal structure contribute to differences in convection over the two seas.

In addition to zonal SST contrasts, the topography of peninsular India plays a major role in monsoon climatology (Rao, 1976; Gadgil, 1977). The Western Ghats coastal mountain range is about 1 km high and runs parallel to the Indian west coast. Rainfall over southern peninsular India in June–September is highest on the windward side of the Western Ghats, with values as high as 600 mm/month (Romatschke and Houze, 2011; Mitra *et al.*, 2013; Shige *et al.*, 2017); there is also an apparent rainfall maximum offshore over the eastern Arabian Sea (Figure 1). The Deccan Plateau to the east of the mountains is in a rainshadow and receives about a tenth of what falls on the Western Ghats during the summer monsoon (Rajeevan *et al.*, 2010; Romatschke and Houze, 2011). Over the Bay of Bengal, rainfall again increases, with high sea surface temperatures, a humid mid-troposphere, and associated mesoscale convective systems (MCSs) and synoptic low pressure systems (Hirose and Nakamura, 2005; Romatschke *et al.*, 2010; Romatschke and Houze, 2011; Virts and Houze, 2016).

It has only recently been established where the maximum rainfall occurs in relation to the Western Ghats (Romatschke and Houze, 2011; Shrestha *et al.*, 2015; Kumar and Bhat, 2017; Shige *et al.*, 2017). Most remote-sensing-based datasets, e.g. the Tropical Rainfall Measuring Mission (TRMM) 3B42 product, a multi-satellite product using microwave, infrared brightness temperature, and precipitation radar along with gauge data, place the maximum rainfall just offshore (Figure 1), while the TRMM radar-only 2A25/3A25 products place the maximum on the windward slopes of the Western Ghats themselves (Romatschke and Houze, 2011; Shrestha *et al.*, 2015; Kumar and Bhat, 2017; Shige *et al.*, 2017). Other remote-sensing rainfall products, such at the Global Precipitation Climatology Project and the Climate Prediction Center Merged Analysis of Precipitation also place

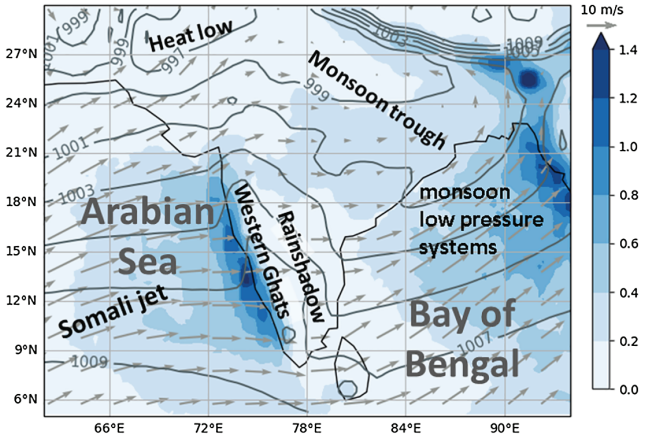

FIGURE 1 Mean rainfall (TRMM 3B42, 1998–2016, blue shading), sea level pressure (ERA-Interim, contours), and 950 hPa horizontal winds (arrows) in South Asia in June. Some of the main features of the monsoon system are labelled

the maximum offshore (e.g. Sperber *et al.*, 2013). It is likely that infrared-based measurements are biased by the advection of anvil clouds in the upper-level easterlies (Figure 2c), shifting the apparent rainfall maximum over the Arabian Sea rather than at the foothills of the Western Ghats (Shige *et al.*, 2017).

Climatologies of radar observations (mostly from satellites) have been used to characterize rainfall over the Western Ghats in more detail. Shrestha *et al.* (2015) showed that the higher mean rainfall over the Western Ghats, compared to offshore, is due to higher rain frequency rather than greater intensity. Kumar and Bhat (2017) and Shige *et al.* (2017) showed that precipitating systems over the Arabian Sea have lower cloud tops than in most other regions where oceanic monsoon flow encounters orography. Kumar and Bhat (2017) also showed that the TRMM convective/stratiform identification algorithm classified rainfall offshore from the Indian west coast as convective more frequently than in other similar regions. Utsav *et al.* (2017) used ground-based weather radar observations at the northern end of the Western Ghats to show that this is most frequently congestus-type convection. While most rainfall upstream of the Western Ghats comes from convective clouds with tops below about 6 km, the most intense rainfall comes from organized large-scale features such as the northward propagation of the tropical convergence zone (Francis and Gadgil, 2006).

The exact mechanisms by which the moist monsoon flow responds to the mountains and produces the observed offshore rainfall patterns are not well understood. Grossman and Durran (1984) used aircraft observations and a two-dimensional model to argue that offshore blocking from the Western Ghats decelerates the onshore flow, forcing convection through large-scale uplift of conditionally unstable air. Smith (1985) proposed that the Western Ghats might simply act as a wall, keeping deep convection to their west, with resultant latent heating acting to destabilize the large-scale flow. Grossman and Durran (1984) did not consider latent heating or

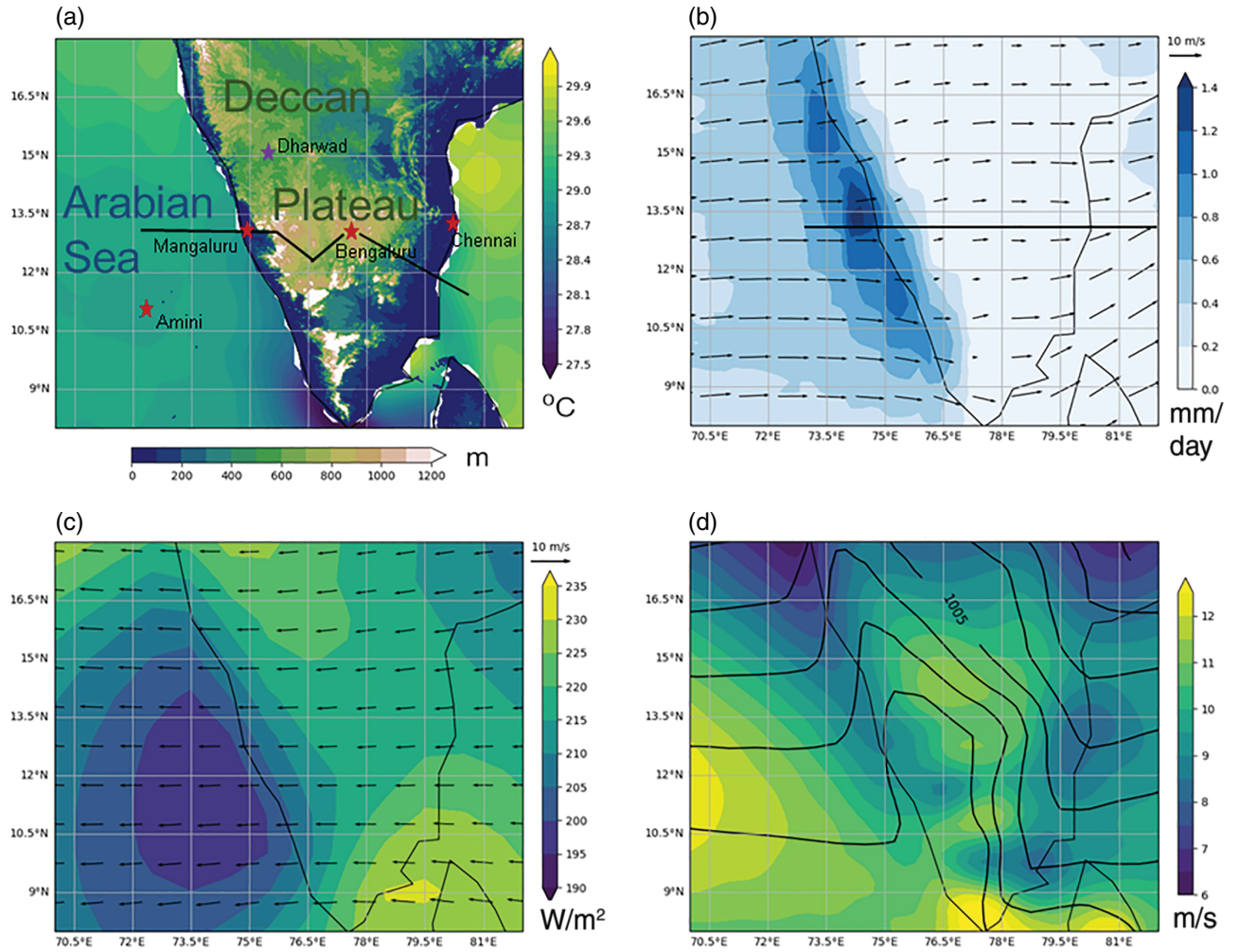

FIGURE 2 June climatology for peninsular India; wind vectors/speed and MSLP from ERA-Interim (1979–2016), and other data are from satellites as described. (a) sea surface temperature (NOAA OISST, 1982–2916) and elevation. Also indicated are locations of radiosonde stations where data are used (red stars), flux tower station (purple star), and flight patterns (schematically indicated by black lines). (b) TRMM 3B42 rainfall (1998–2017; blue shading, mm/day) and 950 hPa winds (arrows). The black horizontal line indicates the location of the cross-section in Figure 3. (c) NOAA NCDC outgoing long-wave radiation (1979–2012; shading, W/m^2) and 300 hPa winds (arrows). (d) Wind speed at 850 hPa (shading, m/s) and mean sea level pressure (contours, hPa)

vertical shear in their simple model of blocking-associated uplift offshore. Ogura and Yoshizaki (1988) found that two-dimensional numerical simulations without shear or surface latent heat fluxes, as in Grossman and Durran (1984), produced rainfall only over the mountain tops, while including vertical shear and latent heating produced widespread precipitation on the windward slopes and hundreds of kilometres offshore as in observations. Recently, Zhang and Smith (2018) found that, in high-resolution simulations of rainfall over the Western Ghats region, offshore rainfall was largely unchanged when the Western Ghats mountains were removed, but it was substantially reduced when latent heating was turned off.

On the Western Ghats themselves, rainfall is thought to be primarily stratiform in association with large-scale orographic lifting. Stratiform-dominated rainfall over the Western Ghats is consistent with observed microphysical properties (Konwar *et al.*, 2014), with observational and modelling studies finding that rainfall on the mountains was more persistent (but less intense) than offshore (Shrestha *et al.*, 2015; Flynn *et al.*, 2017), and with the modelling study of Zhang and Smith (2018), which found that rainfall over the mountains was maintained even with latent heating turned off.

Despite substantial efforts from modelling centres, many climate models have a large dry bias over the Indian subcontinent and a wet bias over the central equatorial Indian Ocean and the Himalayan foothills (Sperber *et al.*, 2013). This bias pattern persists despite targeted efforts at model improvement (e.g. Saha *et al.*, 2014; Walters *et al.*, 2017). The range of space- and time-scales involved in the monsoon add to the difficulty in diagnosing the problems and determining pathways to improvements. Some of the bias has been linked to cumulus parametrization: Willetts *et al.* (2017) found that high-resolution simulations of monsoon rainfall with deep convective parametrization turned off had a smaller overall rainfall bias and a better diurnal cycle of rainfall relative to observations than simulations of the same resolution with

TABLE 1 Overview of all Bengaluru-based flights in INCOMPASS. Daytime flights were typically 1100–1500, evening flights were about 1700–2200, and the night flight was about 2100 to 0200 (all local time)

Flight	Date	Time of day	Direction	Conditions
B958	13 June	Day	Transit from North India	Relatively dry
B959	21 June	Day	Arabian Sea	Widespread rain
B960	22 June	Day	Bay of Bengal	Recent anomalous rainfall over land
B961	23 June	Day	Arabian Sea	Recent heavy rainfall
B962	23 June	Evening	Arabian Sea	Diurnal clearing
B963	25 June	Night	Arabian Sea	Offshore rainfall retreating
B964	26 June	Day	Arabian Sea	Isolated convection
B965	26 June	Evening	Arabian Sea	Isolated convection
B966	27 June	Day	Bay of Bengal	Relatively clear conditions
B967	28 June	Day	Transit to North India	Widespread MCS over central India

parametrization. However, rainfall biases in the South Asian monsoon are also linked to circulation biases. In coupled models, low Arabian Sea SST biases weaken moisture transport in the Somali jet, reducing monsoon rainfall over India (Levine and Turner, 2012; Levine *et al.*, 2013). Insights into the dynamics and thermodynamics of the onshore flow, and what sets the spatial distribution of rainfall, will help guide model improvements.

Open questions remain about the physical processes that models are failing to capture. How is the circulation modified by the sea-to-land transition and orography? What is the boundary-layer structure and variability associated with this circulation? How do these structures in circulation and boundary-layer thermodynamic properties influence the convection and rainfall?

In order to address these questions, we need, among other things, more observations of monsoon circulation. Previous Indian summer monsoon field experiments focusing on atmospheric circulation are described by Bhat and Narasimha (2007). Some of these campaigns have included aircraft observations (e.g. Krishnamurti, 1985; Rao, 2005; Sikka, 2005; Kulkarni *et al.*, 2012) . Grossman and Durran (1984) used data from the Monsoon Experiment (Krishnamurti, 1985) to argue that offshore rainfall is caused by orographic blocking. Maheskumar *et al.* (2014) used the cloud imaging probe data from the 2009 Cloud Aerosol Interaction and Precipitation Enhancement Experiment (Kulkarni *et al.*, 2012) in combination with reanalysis to diagnose deep convective and stratiform rainfall offshore from the Western Ghats, and argued that slow updraughts allow warm rain processes to efficiently produce heavy precipitation on the Indian west coast. Aircraft campaigns such as these provide valuable insights into the physical processes in a region, and the Western Ghats region has been undersampled relative to its importance for monsoon rainfall.

In 2016, the joint UK–India project on Interaction of Convective Organization and Monsoon Precipitation, Atmosphere, Surface and Sea (INCOMPASS) carried out a field campaign to make new measurements of the Indian monsoon. INCOMPASS installed permanent, ground-based instruments at a number of strategic sites throughout India (two in the Western Ghats) and performed high-frequency radiosonde launches in northern India as well as more than 90 hr of research flight time in May–July with the Facility for Airborne Atmospheric Measurement (FAAM) aircraft, the British Aerospace (BAe) 146.

The INCOMPASS aircraft campaign included an intensive observing period (IOP) in late June based in the city of Bengaluru, during which we carried out 35 hr of measurements of the dynamic and thermodynamic structure of the monsoon over south India over ten flights, listed in Table 1. In this paper we focus on aircraft observations from six flights over the Western Ghats and adjacent Arabian Sea, and address the following questions:

- How did the spatial patterns of convection and circulation – over land and sea – change according to the synoptic evolution?
- How did physical parameters such as SST and Froude number change as the intensity of rainfall offshore changed?
- What were the zonal and vertical structures in the boundary layer offshore, and what was their temporal evolution?

Section 2 describes the data used in this study. Section 3 provides an overview of the conditions during the IOP, including tropical wave activity, synoptic-scale flow, the evolution of zonal rainfall contrasts, and time-mean aircraft observations of the same region over multiple days. Section 4 presents physical parameters relevant to different hypotheses on the cause of offshore rainfall. Section 5 shows observations of the zonal contrasts in the low-level onshore flow. In section 6 we show the relationship of the large-scale flow to the diurnal cycle at a flux tower site in the Western Ghats. Section 7 summarizes the results and suggests next steps for improving understanding of the physics of this region.

2 | DATA

2.1 | Description of INCOMPASS data

In this study we mainly focus on data collected by the BAe-146 aircraft. Table 2 describes the aircraft data used in this paper. We focus on basic meteorological data:

TABLE 2 Aircraft observations used in this paper

Quantity measured	Instrument	Notes
Temperature	Non-deiced Rosemount mount Goodrich Total TEMPERATURE Sensor	Less prone to drift than de-iced sensor
Pressure	Static pressure from aircraft RVSM system	
Height	Radar altimeter	Only used over sea with pressure > 900 hPa
Humidity	Water Vapour Sensing System II, Rosemount inlet	Fast response, not prone to flooding
Zonal wind speed	GPS Inertial Navigation (GIN) unit, turbulence probe	
Meridional wind speed	GIN unit, turbulence probe	Bad data replaced with GIN-only v

temperature, pressure, humidity, and zonal and meridional winds. Both de-iced and non-de-iced temperature sensors are on the BAe-146; we chose to use the non-de-iced sensor because it is less prone to drift and because we observed errors in the de-iced sensor during flights. The aircraft has several humidity instruments; we chose to use the Rosemount Water Vapour Sensing System-II because of its fast response time (Vance *et al.*, 2015). Winds were derived from a combination of the aircraft GPS Inertial Navigation (GIN) unit along with the turblence probe on the aircraft nose. The turbulence probe is subject to errors in icing conditions. We found a few instances in which the GIN-turbulence probe estimate of meridional wind had obvious errors (e.g. shifts from about −8 to 40 m/s over a few hundred metres); in those instances the wind field was replaced with the otherwise less accurate GIN-only wind estimate. We mostly used pressure as our vertical coordinate for the data, but for very low elevation runs (straight level portions of a flight) over the ocean we also show the height as detected by the aircraft radar altimeter, which is more accurate than using pressure in the boundary layer but is subject to large error at higher elevations.

INCOMPASS was not permitted to drop sondes during flights, so flight plans included multiple flight track profiles between 30 m and about 7,000 m above the sea surface and between about 150 and 7,000 m above the land surface. We performed six flights to the west over more or less the same flight path, as well as two to the east, indicated schematically in Figure 2a. The combination of aircraft profiles and repeat flights over the same path helps make up for the lack of dropsondes in gathering data on the zonal structure and synoptic evolution of the onshore flow.

INCOMPASS also included the installation of several permanent flux tower sites, two of which are located in the Western Ghats (Figure 2a). These flux towers measure soil moisture, 2 m temperature and humidity, 10 m winds, surface rainfall, and surface fluxes of sensible heat, latent heat, and long-wave and short-wave radiation (Ward *et al.*, 2013). The southernmost of these (Berambadi) was not operational during the IOP, but we use and present data from the northern location, Dharwad.

INCOMPASS data will be publicly available starting July 2018. Access to the data can be obtained from the Centre for Environmental Data Analysis[1].

[1]http://www.ceda.ac.uk/data-centres; accessed 4 January 2019

2.2 | Other data used

In addition to *in situ* aircraft and flux tower data, we used reanalysis and satellite observations.

We used the European Centre for Medium-Range Weather Forecasting Interim Re-analysis (ERA-Interim; Dee *et al.*, 2011) to examine the synoptic-scale flow over the course of the IOP. We also characterized the large-scale environment with radiosonde observations, launched from stations at Amini Island in the Arabian Sea, Mangaluru on the west coast, Bengaluru in central South India, and Chennai on the east coast (Figure 2a). Radiosonde observations were provided for the INCOMPASS project at high resolution from the India Meteorological Department where available, and otherwise are from the University of Wyoming website[2].

We used several satellite datasets in this study. For SST, we used the National Oceanic and Atmospheric Administration Optimum Interpolation Sea Surface Temperature (NOAA OISST[3]; Reynolds *et al.*, 2007), available daily at 0.25° resolution. For outgoing long-wave radiation (OLR) we used the India Space Research Organisation's Kalpana satellite[4]. For brightness temperature, we used EUMETSAT's Meteosat 7 data[5]. For rainfall means over multiple years we used the TRMM 3B42 version 7 product (Huffman *et al.*, 2007), which is three hourly and at 0.25° resolution. For rainfall during the IOP, we used the Integrated Multi-satellite Retrievals for GPM (IMERG) Version 4, which combines microwave and infrared data from the Global Precipitation Measurement (GPM) satellite constellation to provide a gridded precipitation estimate at 0.1° resolution every 30 min[6]. We also used data from the GPM Ku-band Precipitation Radar to examine the vertical structure of precipitating systems during the IOP, and the TRMM Precipitation Radar to provide a long-term mean of that structure. Finally, we briefly used Version 3 of the Goddard Satellite-based Surface Turbulent Fluxes near-global sea surface latent heat flux climatology[7] (Shie *et al.*, 2012).

[2]http://weather.uwyo.edu/upperair/sounding.html
[3]https://www.ncdc.noaa.gov/oisst
[4]https://mosdac.gov.in
[5]http://archive.eumetsat.int/
[6]https://pmm.nasa.gov/data-access/downloads/gpm
[7]https://mirador.gsfc.nasa.gov/; all accessed 4 January 2019

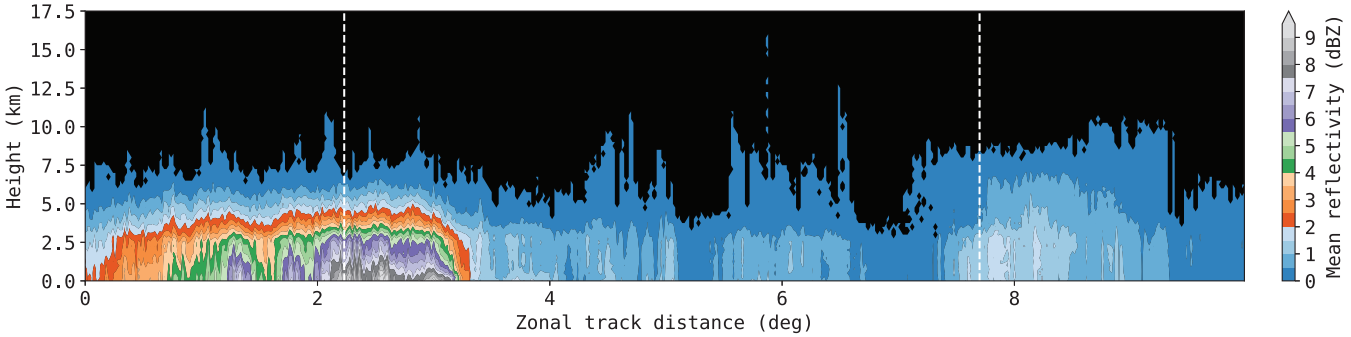

FIGURE 3 TRMM Precipitation Radar reflectivity (Arabian Sea to Bay of Bengal) for all overpasses 21–28 June, 1998–2014. averaged from 12°N to 14°N over South India. Dashed vertical lines indicate locations of west and east coasts. The location of the cross-section is indicated in Figure 2b

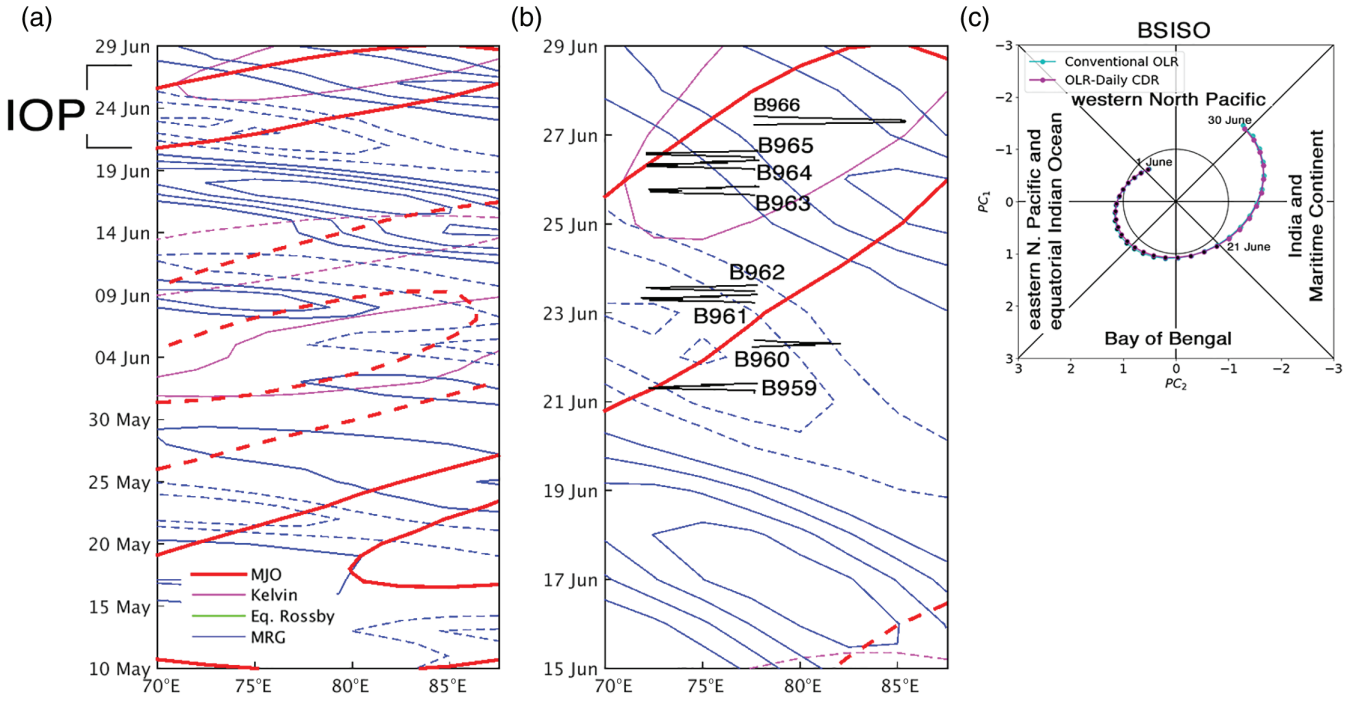

FIGURE 4 (a) Hovmöller diagram of OLR projections at 12.5°N onto tropical wave modes for May and June 2016, and (b) expansion of part of (a) for the IOP. Solid lines indicate negative OLR anomalies and dashed lines indicate positive OLR anomalies. Contour interval is 10 W/m^2, with absolute anomalies greater than 50 W/m^2 omitted. Flight patterns (black lines) are overlaid for reference. (c) Wheeler–Hendon diagram of the BSISO index of Kikuchi *et al.* (2012). The index is calculated with two different datasets: NOAA's daily interpolated (conventional) OLR and the NCDC's outgoing long-wave radiation–daily climate data record (OLR-Daily CDR)

2.3 | Tropical modes

We used the algorithm of Roundy (2012) to project interpolated NOAA Earth Systems Research Laboratory OLR (Liebmann and Smith, 1996) onto equatorial wave patterns in order to characterize tropical wave activity during the campaign. This algorithm produces a gridded time series of coherent structures in prescribed zonal wavenumber/frequency bands associated with a range of tropical wave modes, including the Madden–Julian oscillation (MJO). Global projections can be viewed at http://www.atmos.albany.edu/facstaff/roundy/waves/ (accessed 4 January 2019).

Additionally, we used the Boreal Summer Intraseasonal Oscillation index of Kikuchi *et al.* (2012) to diagnose OLR patterns associated with that summertime mode, which is characterized by a northward propagating, northwest to southeast tilted band of convection extending from the Arabian Sea to the western Pacific.

3 | THE LARGE-SCALE ENVIRONMENT

3.1 | June climatology

Figure 1 shows the major features of the monsoon climatology in June. The Somali jet, the lower-tropospheric southwesterly flow, transports moisture as it crosses the Arabian Sea and brings the monsoon onset first in early June to Kerala, the southwesternmost state in India. As the monsoon trough develops throughout June, the monsoon rains progress from the Western Ghats mountains along the peninsular west coast,

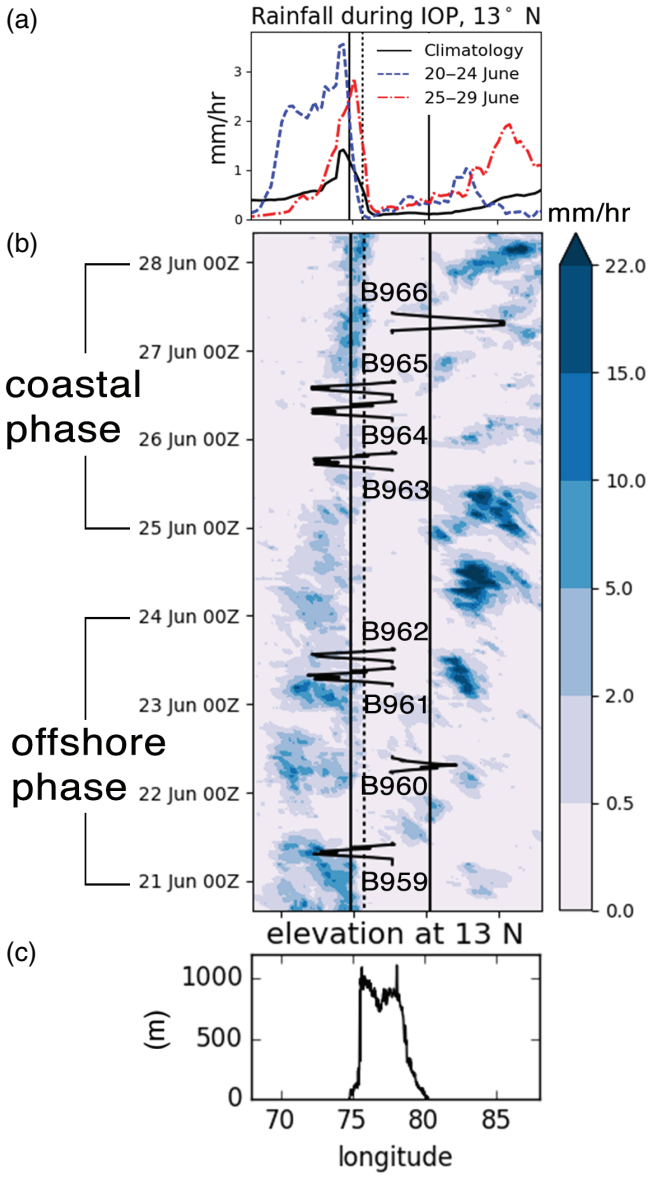

FIGURE 5 (a) Mean rainfall from 12°N to 13°N from TRMM 3B42 over the indicated time periods. (b) Hovmöller diagram of IMERG rainfall (mm/hr) averaged over 12–14°N during the IOP. Flight paths are overlaid in black. Note the nonlinear colour scale. (c) Topography elevation profile at 13°N. Solid black lines on (a) and (b) indicate the coasts, and the dashed line indicates the peak of the Western Ghats

to the northeast via the Bay of Bengal, and then finally to the northwest heat low region in July. The highest rainfall in the monsoon occurs on the Meghalaya Plateau in northeastern India and in the vicinity of the Western Ghats, where the low-level monsoon flow in the Somali jet first encounters land.

Figure 2 focuses on the region in this study, showing climatological conditions over peninsular India in June from satellite observations and reanalysis. The Arabian Sea SST (Figure 2a) is typically slightly below 29°C, and is slightly lower at the coast than at 72°E. This cooling is due to coastal upwelling in response to the northerly component of the low-level winds (Findlater, 1969), and is stronger near the southern tip of India than in the location of our flights. During the IOP, eastern Arabian Sea SSTs were similar to climatology, with coastal SST in the location of the flights about 0.3°C lower than at 72°E (not shown).

There is a slight northerly component to the low-level onshore flow south of about 12°N (Figure 2b), consistent with the blocking created by the Western Ghats (Figure 2d). While rainfall is greatest on the windward side of the Western Ghats (Figure 2b), OLR is greatest further offshore as cirrus clouds are advected with the upper-level easterlies (Figure 2c). Deceleration of the low-level monsoon flow, which Grossman and Durran (1984) argued was key to widespread rainfall offshore, is seen in Figure 2d, with 850 hPa wind speeds dropping from about 12 m/s over the open ocean to about 8 m/s near the coast.

Figure 3 shows a cross-section at 13°N (the location of the flights) of climatological mean radar reflectivity from the TRMM Precipitation Radar. These cross-sections highlight the locations of highest reflectivity, starting about 200 km offshore from the west coast to the top of the Western Ghats mountains. The climatology shows that precipitating systems over the Bay of Bengal are deeper than those over the Arabian Sea, but produce less rainfall.

3.2 | During the IOP

In this section we provide an overview of the synoptic conditions during the IOP including tropical wave activity, the evolution of the spatial pattern of rainfall, and the evolution of the large-scale flow from reanalysis.

3.2.1 | Satellite observations of OLR and rainfall

Figure 4 shows the projection of OLR anomalies at 12.5°N onto equatorial wave patterns leading up to and during the IOP, calculated as described in Roundy (2012); we have also reproduced their figure style. The dominant patterns were associated with the MJO and with mixed Rossby-gravity waves. An active phase of convection with MJO-like patterns propagated through the region during the IOP. The MJO is weaker in India in Northern Hemisphere summer than in winter (Annamalai and Sperber, 2005), so this MJO signal may indicate the passage of an active phase of the 30–50 day northeastward propagating Boreal Summer Intraseasonal Oscillation (BSISO; e.g. Annamalai and Slingo, 2001). Kikuchi *et al.* (2012) identified separate MJO and BSISO modes and found that the BSISO mode dominates June to October. Their index (Figure 4c) shows that the BSISO was active over India during the campaign. The MJO index of Wheeler and Hendon (2004) showed a similar pattern during the IOP (not shown), but the bimodal index of Kikuchi *et al.* (2012) generally captures a higher fraction of the OLR variance.

Figure 5 shows the time-evolution of rainfall in the location of the flights over the course of the IOP. For the first few days of the flights, heavy precipitation fell offshore over the Arabian Sea. The rainfall over the east coast rain shadow

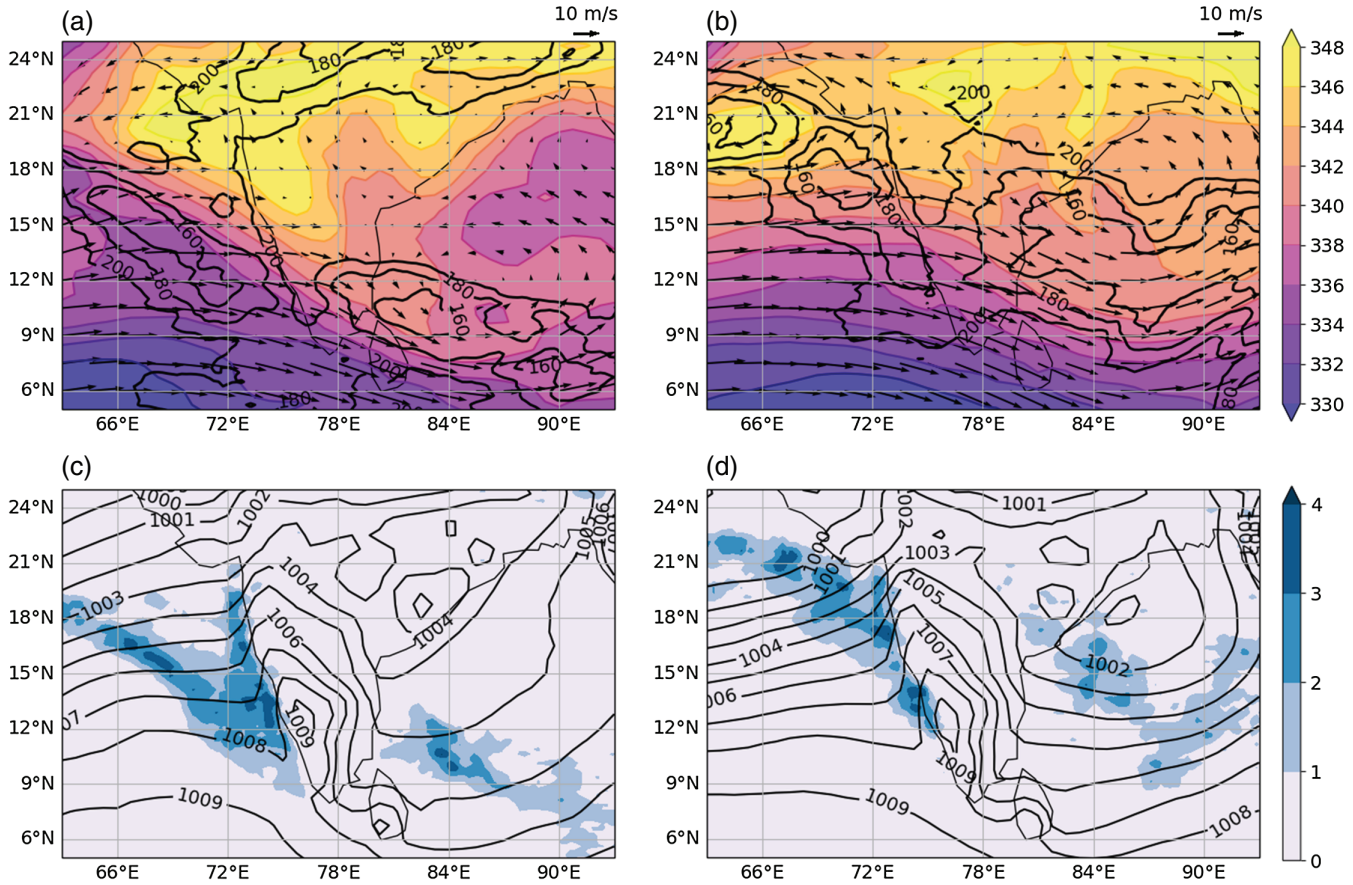

FIGURE 6 Synoptic environment over the course of the IOP; 3-day averages from (a, c) 0000 UTC 21 June to 1800 UTC 23 June, and (b, d) 0000 UTC 25 June to 1800 UTC 27 June. (a, b) Averages of outgoing long-wave radiation (black contours, interval 20 W/m^2 with contours > 200 omitted) from the Kalpana satellite with wet bulb potential temperature (shading, K) and horizontal winds at 700 hPa (arrows) from ERA-Interim. (c, d) TRMM 3B42 rainfall (shading, mm/hr) and mean sea level pressure (contours, hPa) from ERA-Interim

was comparatively weak, but represented a positive departure from climatology (Figure 5a). From 23 to 25 June, substantial rain fell over the Bay of Bengal in association with the monsoon low pressure system (Figure 6), while at the same time rainfall began to subside over the Arabian Sea. This evolution in the spatial rainfall pattern was associated with the northward movement of the southeast-to-northwest oriented band of rainfall over the Arabian Sea (Figure 6) and Bay of Bengal; this band itself was associated with the active phase of the BSISO.

Over the course of the IOP, the rainfall shifted from offshore to directly over the Western Ghats. Figure 5b was made with IMERG rainfall to allow for high resolution, but when done with TRMM 3B42 (a), comparison to the 15-year climatology of TRMM can be made. This comparison revealed that, while heavy rain fell over the Arabian Sea during the first few days of the IOP, rainfall was suppressed at that time compared to climatology over the Western Ghats. By the end of the IOP, substantial rain was falling over the Western Ghats and the adjacent Arabian Sea was relatively dry. This pair of 3-day periods (21–24 June and 25–28 June) represent two different rainfall regimes over the Western Ghats and are also the two periods during which all flights occurred. We will therefore examine the conditions for flights from the first 3-day period and the last 3-day period separately. We will refer to these two distinctive 3-day periods as the "offshore" and "coastal" periods, respectively.

The high resolution of IMERG data makes it possible to visualize the propagation of storms between the Indian west coast and the open Arabian Sea. In the offshore phase, patches of heaviest rainfall from IMERG propagated to the west with a speed of roughly 5 m/s, which is comparable to, or slightly less than, the 300 hPa climatological easterly wind speed shown in Figure 2c. Eastward propagation from the Arabian Sea to the coast did not occur. A diurnal pattern in precipitation during the offshore phase is also apparent, with the heaviest rainfall occurring in the morning (0000 UTC is 0530 local time) and the least rain falling in the evening. Flynn *et al.* (2017) attribute this diurnal cycle to a weak land breeze at night producing convergence in the morning.

3.2.2 | The synoptic-scale flow

Figure 6 shows the synoptic environment from ERA-Interim and satellite observations averaged over the offshore and coastal periods. Over the Bay of Bengal, indicators of convection – rainfall in blue in (c, d) and OLR contours in (a, b) – were most prominent in the southwest quadrant of

the low pressure system. Over the Arabian Sea, there were two bands of precipitation during the offshore phase: the northwest-to-southeast oriented band discussed above, with a similar band in OLR; and another band of rainfall that hugged the west coast and had a relatively weak OLR signal. The weak OLR anomalies over the coastal rainfall band indicate that this rainfall is from clouds of moderate vertical extent. During the coastal phase, the offshore band of precipitation merged with the coastal rainfall band and a vortex in the northern Arabian Sea developed.

Figure 6 also shows the decrease in mid-tropospheric humidity over almost all of India during the coastal phase in association with enhanced westerlies over the Arabian Sea bringing relatively dry air, including a plume of very dry mid-level air originating over the western Arabian Sea. Aircraft observations of this mid-level dry air incursion will be discussed later.

3.2.3 | Time-mean aircraft and radiosonde observations

To examine the thermodynamic and dynamic structure of the region, Figure 7 shows cross-sections of potential temperature (θ), specific humidity (q), and zonal winds (u) from aircraft and radiosonde observations averaged over the offshore and coastal periods discussed above. We included radiosonde observations to provide additional information about vertical structure, given the lack of dropsondes in the campaign. Potential temperature and specific humidity are plotted in Figure 7 as a departure from horizontal, time-means over the course of the IOP.

Some of the features were climatological: the east was warmer than the west, especially near the surface. But many features changed between the two periods. The boundary layer over the Arabian Sea was cooler and drier during the offshore phase than the coastal phase. During the offshore phase θ and q were particularly high over the Arabian Sea between about 600 and 400 hPa. In the lower troposphere, temperatures over the Arabian Sea during the offshore phase were consistently cooler than in the coastal phase and further to the east. By the coastal phase of the IOP, most of the region had higher potential temperature than the offshore phase.

There is an immediately noticeable difference between aircraft and radiosonde observations of specific humidity (Figure 7c,d), with radiosonde q generally being higher than aircraft observations, especially in the lower troposphere. We attribute this discrepancy primarily to the slow response time of the humidity sensor in the radiosondes. Aircraft observations show that mid-tropospheric q over the Arabian Sea dropped substantially between the offshore and coastal phases, showing the far-reaching effects of the dry air intrusion.

Figure 7e,f further show that zonal winds were weaker during the offshore phase, when there was a northerly wind component associated with the Bay of Bengal low pressure system (Figure 6a). West of 78°E, winds shifted from westerly to easterly at about 500 hPa in the westernmost region sampled. The critical layer ($u = 0$ line) sloped down to nearly 600 hPa over land. During the coastal phase, low-level westerlies were stronger, and the shift to easterlies occurred at about 400 hPa, with more zonal uniformity in the height of the critical layer than during the offshore phase.

Figure 8 shows plots equivalent to Figure 7 for ERA-Interim. We include these because ERA-Interim qualitatively captures the same features seen in Figure 7, but some of those features, such as the height of the critical layer, are easier to see. The critical layer sloped down toward the east more prominently in the offshore phase than in the coastal phase, and was also anomalously warm (Figure 8a). These features agree with the simulations of Klemp and Lilly (1978; their figures 20–21), who calculated numerical solutions for hydrostatic, stably stratified flow over a Gaussian ridge and saw large downward displacement of dry adiabats just below the critical layer above the topographic feature. Ogura and Yoshizaki (1988) performed a suite of simulations testing the effect of marine surface fluxes, vertical shear, and latent heating on the distribution of rainfall in flow over mountains similar to the Western Ghats. When vertical shear was included, the resulting perturbations to potential temperature and zonal wind (Ogura and Yoshizaki, 1988; their figure 13) resembled those of Klemp and Lilly (1978) as well as those of the offshore phase in Figures 7 and 8. Furthermore, the mid-tropospheric perturbations in potential temperature and zonal wind in the coastal phase in Figure 8, with a much higher critical layer, resemble the uniform westerly wind experiments of Ogura and Yoshizaki (1988; their figure 3), with a region of enhanced zonal flow above the mountain and dipping downward to the east, and a region of weakened zonal flow above. The similarities between the observed and modelled horizontal perturbations in zonal winds and potential temperature suggest that these perturbations are set by the gravity wave response to flow over orography under different vertical shear conditions, which are themselves largely determined by the large-scale flow.

3.2.4 | Vertical and horizontal structure of precipitation over the Arabian Sea

In this section we examine the vertical structure of precipitation during the IOP as seen by the GPM Ku-band Precipitation Radar.

Figure 9 shows the structure of clouds and precipitation over the Arabian Sea during the both phases. Meteosat 7 brightness temperature shows where the deepest clouds are. Particularly on the first few days of the offshore phase, a widespread region of cold cloud tops is seen over the eastern Arabian Sea. These regions have brightness temperatures as low as 200 K. Observers on the BAe-146 consistently noted that the tops of most precipitating cloud systems were below 400 hPa throughout the campaign (the highest flight level), with cirrus at higher levels. This observation is consistent

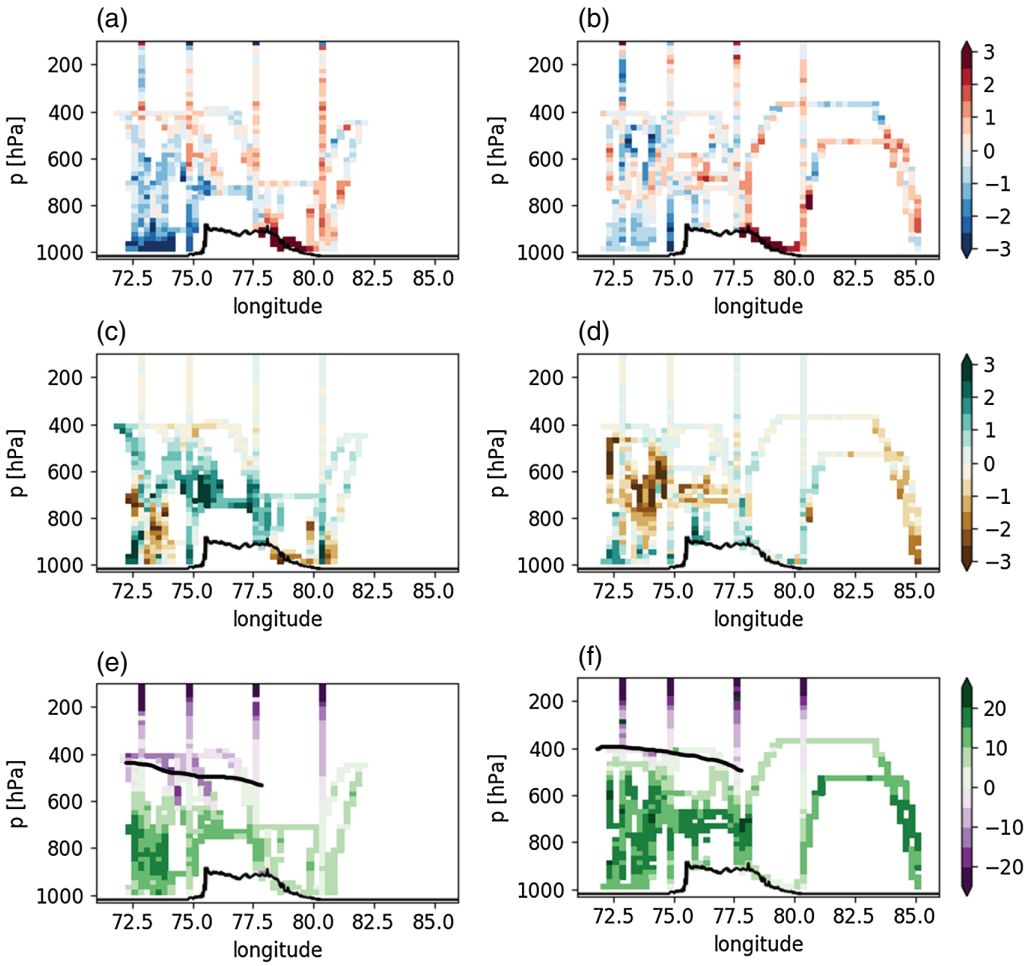

FIGURE 7 Time-mean cross-sections of (a, b) potential temperature (K), (c, d) specific humidity (g/kg), and (e, f) zonal wind speed (m/s) from (a, c, e) the beginning of the IOP (offshore period) and (b, d, f) the end of the IOP (coastal period), combined from aircraft and radiosonde observations. Potential temperature and specific humidity are departures from horizontal time means. The thin black line indicates topography at 13°N. In (e, f) the upper edges of the critical layer have also been indicated by black lines. Bin sizes are 0.25 degrees longitude by 20 hPa. With flight speeds of about 100 m/s, ascent/descent rate of 5 m/s during profiles, and sample speeds of 1 Hz, there were at least 250 samples per longitude bin per flight and 40 samples per pressure bin per flight when the aircraft was profiling

with previous findings that monsoon rainfall over the eastern Arabian Sea comes from clouds with fairly low tops and often involve warm rain processes (e.g. Shige *et al.*, 2017). We infer that the very cold cloud tops over the eastern Arabian Sea in Figure 9 are mostly from cirrus clouds, with warmer precipitating cloud systems below. GPM overpasses, indicated by the swaths in the plan-view panels, provide the horizontal patterns of precipitation while the panels directly below show the vertical structure of precipitation echos seen by the GPM Ku-band radar. On 20 June the overpass captured coastal rainfall, which was fairly widespread but not heavily precipitating. Weak stratiform rain fell just offshore while convective (likely congestus) rain fell on the coast.

In contrast, when GPM passed over the region on 22 June, it sampled a broad stratiform precipitation complex hundreds of kilometres in scale. The precipitation can be identified as stratiform due to the bright band of highest intensity reflectivity between 4 and 5 km height (Houze, 1997; 2014, Chapter 6). By the following day, the offshore regime was transitioning to a mix of convective and stratiform rainfall, with precipitating systems much smaller in horizontal scale than they had been in the days previously. These precipitation elements are typical of the region upstream of the Western Ghats (Houze *et al.*, 2015).

The GPM overpasses over the Arabian Sea during the coastal phase (Figure 9, bottom two rows) captured the structure of precipitation both in the northward moving band of heavy rainfall and in the smaller precipitating systems that remained after it passed. These features generally appear more convective in nature than the overpasses in the offshore phase; however the overpass on 25 June was well north of the region of study. The overpass on 25 June captured deep convection, some with cores 20 km wide on the trailing edge of the precipitating complex. The rainfall on the coast on 26 June was more intense and more convective than on the 20 June overpass.

This section has given an overview of the large-scale conditions during the IOP. The northward propagation of an active phase of the BSISO produced two distinctive phases of rainfall over the Western Ghats and adjacent Arabian Sea. The offshore phase was characterized by heavy rainfall over the

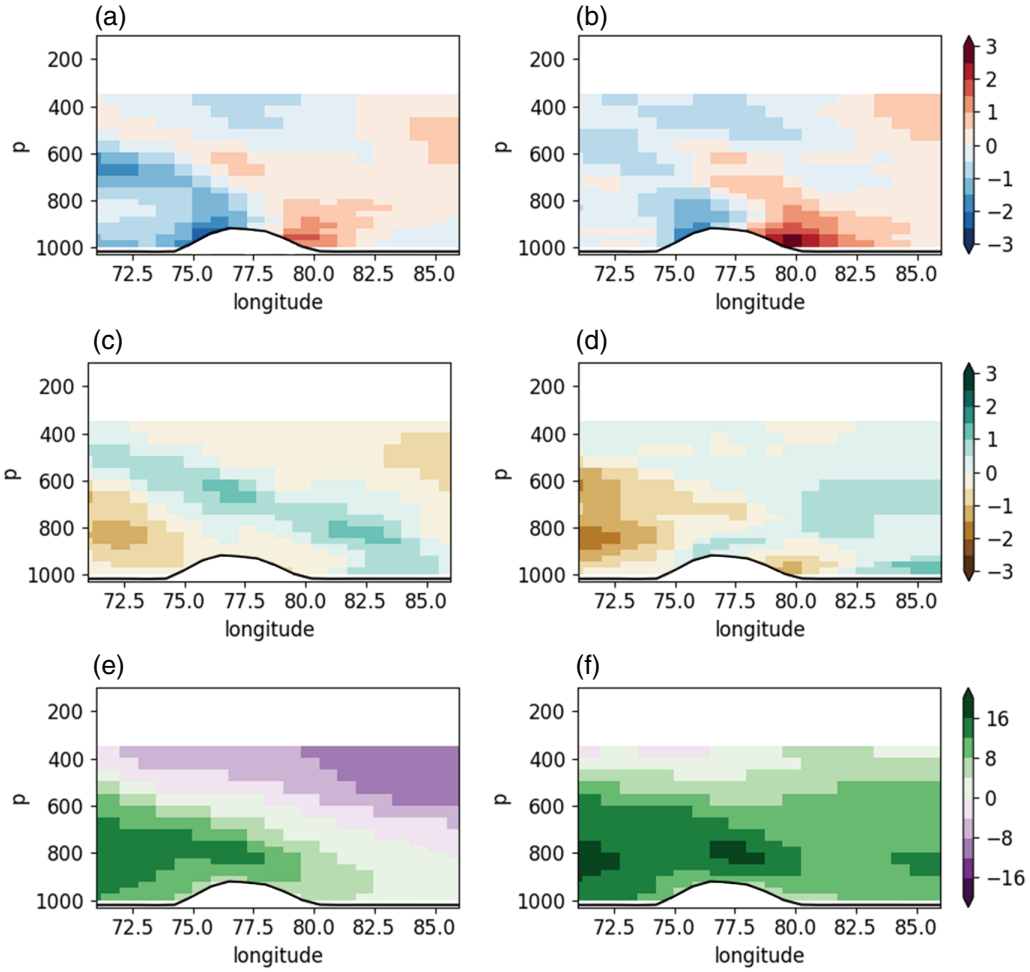

FIGURE 8 Time-mean cross-sections as in Figure 7, but from ERA-Interim. Thin black line indicates topography from ERA-Interim

eastern Arabian Sea and relatively light rainfall over the Western Ghats. As the rainfall band propagated northward, this pattern was reversed. The coastal phase was characterized by a mid-tropospheric dry intrusion and enhanced westerlies in the onshore flow.

4 | CONTROLS ON OFFSHORE RAINFALL

As discussed in section 1, the physical processes responsible for heavy rainfall far upstream of the Western Ghats remains an outstanding question after decades of research. Many attribute it to blocking following Grossman and Durran (1984), but others such as Ogura and Yoshizaki (1988) and Zhang and Smith (2018) have argued against blocking as the primary mechanism. This IOP is too short, and the observations too incomplete, to provide strong evidence for or against any of the possible mechanisms. However, we can note which mechanisms are consistent with observations during the campaign. Here we address the association of SST, convective available potential energy (CAPE), orographic blocking, and mid-tropospheric humidity with the changing intensity of offshore rainfall during the IOP. Table 3 summarizes some of the relevant observations for our six flights over the Arabian Sea.

4.1 | Sea surface temperature

SST is an important control on rainfall over the tropical oceans. Zhang and Smith (2018) argue that SST is important for rainfall upstream of the Western Ghats, with higher SSTs coinciding with heavier offshore rainfall. During the IOP, higher SSTs were generally observed during the offshore phase; however, the wettest day (21 June) had relatively low SSTs. The difference between the highest and lowest mean SST over the course of the IOP was 0.23°C.

4.2 | Convective available potential energy

While CAPE is a well-known predictor of deep convection over land, especially in the extratropical summer, it is often anti-correlated with rainfall over tropical oceans (e.g. Thompson *et al.*, 1979; Mapes and Houze, 1992; Lin and Johnson, 1996). This anti-correlation was the case for offshore rainfall during the IOP (Table 3), where CAPE was considerably higher upstream (Amini) and at the coast (MGLR) during the

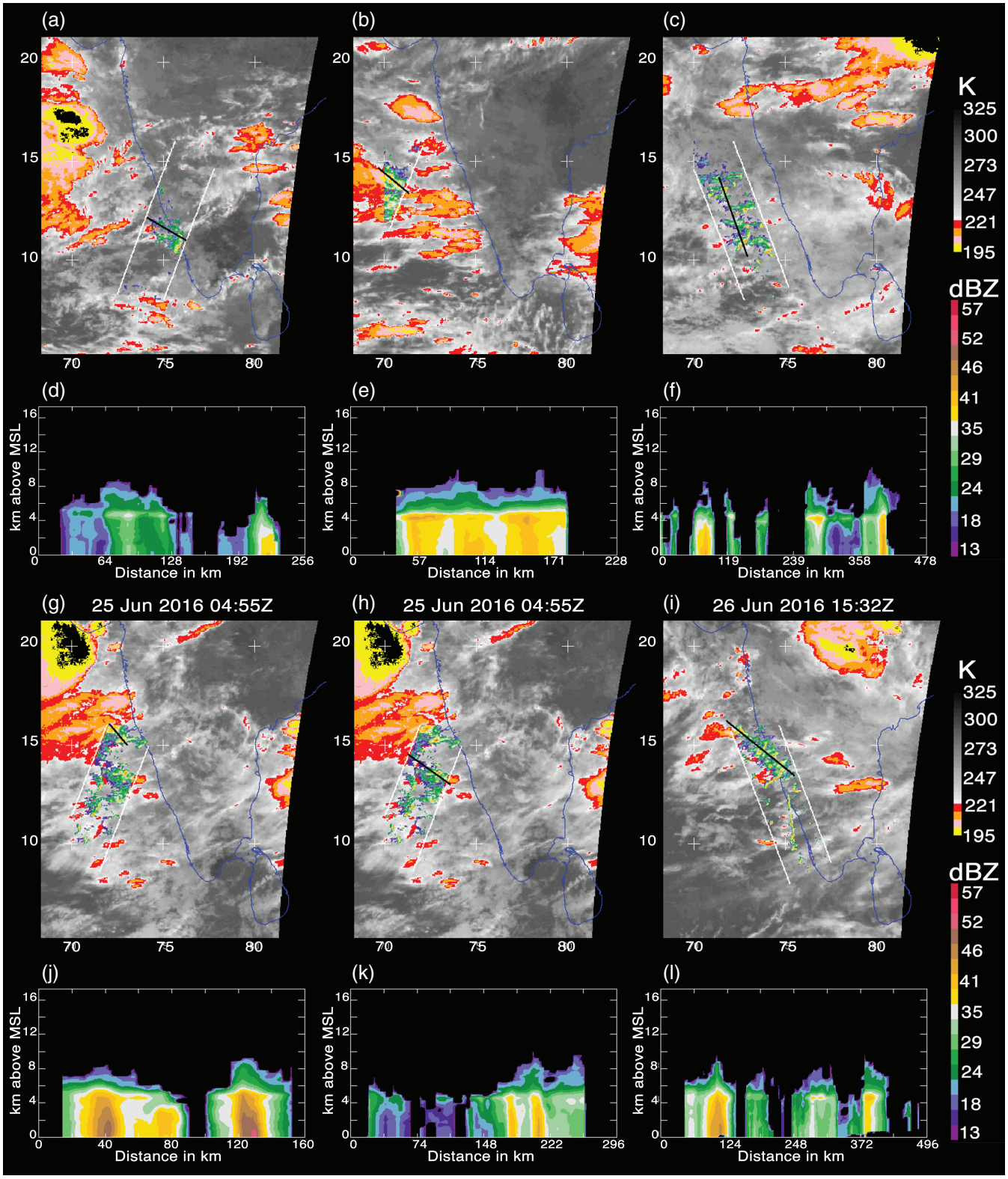

FIGURE 9 (a–c, g–i) Meteosat 7 brightness temperature (greyscale and red colours, K) at times of selected GPM overpasses during the IOP. GPM Ku-band precipitation radar reflectivity (multi-colours, dBZ) at 2 km above mean sea level is overlaid in the swath. (d–f, j–l) reflectivity (dBZ) cross-sections at locations indicated by black lines in the swaths above. All cross-sections are drawn west to east. (a–f) are from the offshore phase and (g–l) are from the coastal phase

TABLE 3 Overview of flights over the Arabian Sea, with some parameters thought to be important for rainfall offshore. Rainfall (mm/hr) is the IMERG average over 12.75–13.25°N, 72–75°E, from 3 hr before the flight to 3 hr after. SST (°C) is from the NOAA OISST daily mean observations over 12–14°N, 70–73°E. Amini and MGLR CAPE (J/kg) refer to the values from the radiosonde launches at Amini Island and Mangaluru respectively (Figure 2a gives locations); for daytime flights the 0000 UTC ascent is used while for evening and night flights the 1200 UTC ascent is used. All radiosonde launches were within 6 hr prior to the time the aircraft reached the region. $U/(Nh)$ is the Froude number of the flow from aircraft observations, assuming the height of the mountains $h = 900$ m, averaged west of 74.5°E and below the 800 hPa pressure level. q_{mid} is the mean specific humidity (g/kg) from aircraft observations west of 74.5°E between 700 and 400 hPa

Flight	Date	Phase	Time of day	Rainfall	SST	Amini CAPE	MGLR CAPE	$U/(Nh)$	q_{mid}
B959	21 June	Offshore	Day	2.3	28.58	889.0	156.7	0.6	6.5
B961	23 June	Offshore	Day	1.1	28.78	510.9	65.5	1.3	6.7
B962	23 June	Offshore	Evening	1.3	28.78	NA	340.6	0.9	6.3
B963	25 June	Coastal	Night	0.2	28.62	NA	175.8	0.9	5.1
B964	26 June	Coastal	Day	0.0	28.55	1370.0	715.0	1.1	3.3
B965	26 June	Coastal	Evening	0.8	28.55	NA	2158.6	1.0	4.5

last few days when there was little rain over the eastern Arabian Sea. High values of CAPE during the coastal phase likely came from increases in boundary-layer humidity, shown in Figure 7 and discussed in more detail in section 5 below. This high humidity may have contributed to heavier rainfall seen over the mountains during the coastal phase, as discussed later in section 6.

4.3 | Blocking

The field $U/(Nh)$, the Froude number, is an indicator of the effectiveness of the mountains of height h in blocking the flow (e.g. Smolarkiewicz and Rotunno, 1989), with blocking indicated by $U/(Nh) << 1$. The Froude number from aircraft observations is shown in Table 3. Here U is the zonal wind speed and N is the Brunt–Väisälä frequency $\sqrt{g/\theta_v(\partial\theta_v/\partial z)}$ where θ_v is the virtual potential temperature. The Froude number is close to one in most cases, indicating that the flow is at most weakly blocked by the mountains. The exception is the first flight, B959, which has a lower Froude number of 0.6 and is also the flight where the most rain fell offshore.

4.4 | Dry intrusion

In the latter half of the IOP, a mid-level intrusion of dry air from the western Arabian Sea surged over the region, shown by the drop in mid-tropospheric water vapour in the last column in Table 3. Of the parameters shown in Table 3, mid-tropospheric specific humidity best captures the transition from the high rainfall values during the offshore phase to the low rainfall values during the coastal phase. The role of dry intrusions in suppressing tropical marine convection has been shown by Mapes and Zuidema (1996) and Parsons *et al.* (2000). Parsons *et al.* (2000) found for observations of the West Pacific warm pool region that suppression of convection by dry intrusions allows the boundary layer to recharge moisture, resulting in very high CAPE values, similar to those in Table 3.

The evolution of the dry incursion is seen in aircraft profiles and radiosondes in Figure 10, plotted as tephigrams. The aircraft profiles, in which the aircraft flew at a constant ascent/descent rate of 5 m/s, substituted for the lack of dropsondes on the campaign. The left column shows profiles west of 73°E, about 150 km offshore, the centre column shows profiles east of 73°E (i.e. within 150 km of the coast), and the right column shows radiosonde profiles from Mangaluru on the coast (Figure 2 gives the location). The radiosondes show nearly saturated profiles up to about 600 hPa in the first three rows, while the aircraft profiles reveal many low dry layers. This discrepancy may be due to the slower response time of the humidity sensor in the radiosonde than the WVSS-II sensor on the aircraft as well as the more horizontal angle of the aircraft profiles compared to the radiosondes.

Both the radiosonde and aircraft profiles show the dry intrusion on the dates of flights B964 and B965. The dry intrusion appears to dip downward toward the east (this can be seen most readily in Figure 7d), which makes it more apparent in the eastern aircraft profiles than the western ones, since the profiles mostly do not go very high.

Of the parameters presented here, SST and mid-tropospheric humidity appear to be most associated with the drop in offshore rainfall over the course of the IOP, with blocking playing a more minor role. The incursion of dry air suppressed convection over the eastern Arabian Sea. However, suppressed convection allowed humidity to build up in the lowest layers of the onshore flow, reflected in the build-up of CAPE seen in Table 3. The stronger, moister onshore flow in turn produced high rainfall on the coast and over the slopes of the Western Ghats, as discussed in more detail in section 6.

5 | BOUNDARY-LAYER STRUCTURE AND EVOLUTION OVER THE ARABIAN SEA

We now turn to a more detailed investigation of the horizontal structure and temporal evolution of the boundary layer offshore. Figure 11 shows observations from low-level runs on all flights over the Arabian Sea. Two of these flights (B961 and B963) were done after dark, so the lowest permissible height flown was 1,000 ft (about 300 m). During the daytime

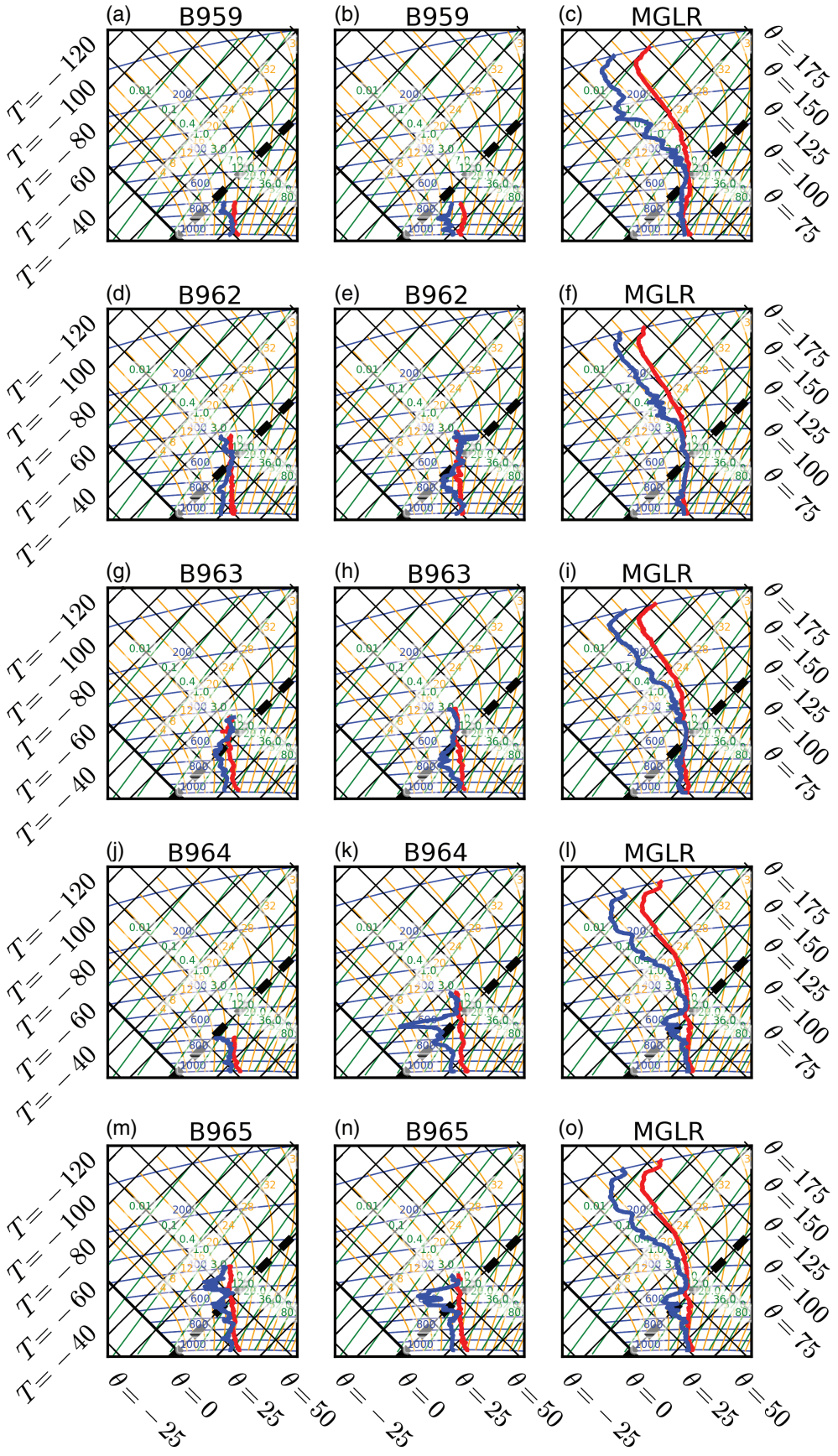

FIGURE 10 Profiles from aircraft ascent/descents for flight B959 (a) west of 73°E, about 150 km off the Indian west coast, (b) east of 73°E but still offshore, and (c) the nearest-time radiosonde ascent from Mangaluru, on the coast (Figure 2a shows locations, Table 3 or Figure 5 give timing of flights). Subsequent rows show corresponding data for other flights; flight B961 is omitted because that flight did not go as far west as the other flights. Red curves indicate temperature, blue curves dewpoint temperature, and bold dashed black lines the freezing level

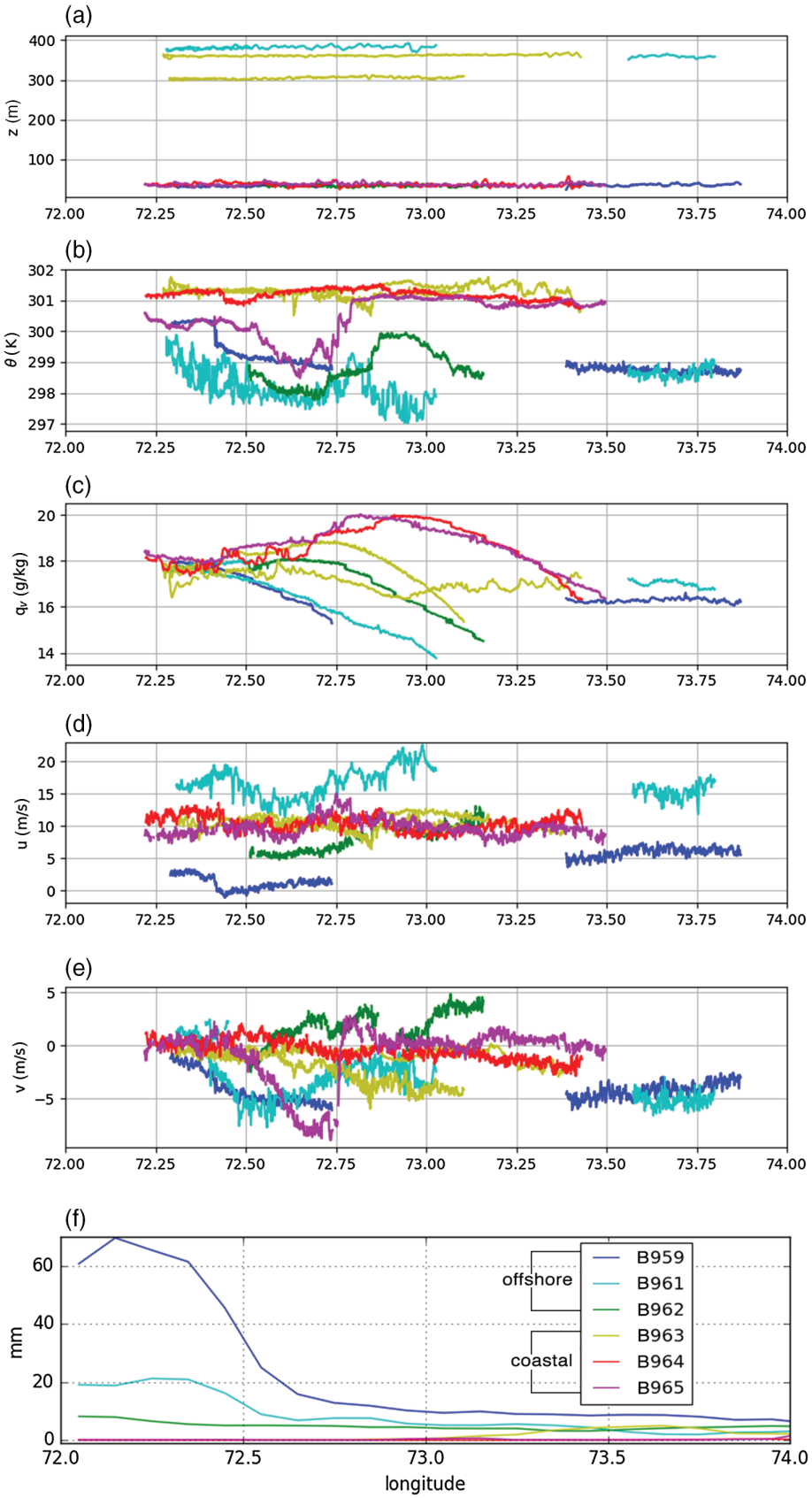

FIGURE 11 Low-level runs over the Arabian Sea: (a) altitude; all flights are at approximately 30 m height except B961 and B963, (b) potential temperature (K), (c) specific humidity (g/kg), (d) zonal wind speed (m/s) and (e) meridional wind speed (m/s). (f) shows the accumulated IMERG precipitation over 12.75–13.25°N during the flights. B959–B962 (blue, cyan, green) are during the offshore phase; B963–B965 (yellow, red, magenta) are during the coastal phase

flights, these low runs were performed at 100 ft, or about 30 m. In all cases the low-level runs shown in Figure 11 were below cloud base, which was estimated from aircraft profiles as ranging from 800 to 2,000 m elevation.

5.1 | Observed characteristics of the Arabian Sea boundary layer

Boundary-layer potential temperature was usually lower during the offshore phase. Boundary layer θ also usually showed more horizontal variability within individual flights and had a wider range across all flights during the offshore phase than it did during the coastal phase. Similar differences in variability and overall range between the two phases are seen in zonal winds, which were almost always about 8–12 m/s during the coastal phase but ranged from 0 to 25 m/s during the offshore phase. (Analysis of the large dip in θ and v during B965 between about 72.5 and 72.75°E suggests that the aircraft flew through a bore or gravity current; this feature is interesting but not relevant to the results presented here.)

The zonal changes in boundary-layer specific humidity proved interesting. At the furthest west point, close to 72°E, the aircraft consistently measured specific humidity of about 18 g/kg. But on every run, at some point there was a substantial drop in humidity to as low as 14 g/kg. This drop occurred regardless of the time of day, synoptic conditions, or altitude (within the mixed layer) of the aircraft, although the location of the moisture drop shifted to the east over the course of the IOP. In flights B959 and B961 the locations of the humidity drops corresponded to locations of gradients in rainfall accumulation over the course of the flight. However, rainfall cannot explain the zonal moisture gradient, as this gradient was also observed on flights in which there was no rainfall.

Furthermore, NOAA OISST observations for the IOP indicate that the magnitude of SST decrease over this region was less than 0.3 K per degree longitude, and that SST increased very near the coast (not shown). The weak decrease in SST approaching the coast cannot, by itself, explain the moisture drop in the low-level onshore flow. The degree to which SST changes explain (or do not explain) the reduction in humidity as the flow approaches the coast is examined quantitatively in section 5.2.

5.2 | Boundary-layer moisture budget

Figure 12 shows that there was a shallow well-mixed subcloud layer observed on most of the flights, especially further offshore. Stevens (2006) argued that a well-mixed subcloud layer may be modelled with a mixed-layer model similar to that used for a stratocumulus-topped boundary layer; however this assumption is best done in the absence of precipitation. We will therefore only apply the following analysis to the two flights in which there was no offshore rainfall: B964 and B965. We take a rough mixed-layer moisture budget approach to better understand the moisture gradient:

$$\frac{\Delta q}{\Delta t} = -u\frac{\Delta q}{\Delta x} - v\frac{\Delta q}{\Delta y} + \frac{LHF}{h} - w_e\frac{\Delta q}{\Delta z}\bigg|_{top} + P_{evap}. \quad (1)$$

Equation 1 represents the approximate budget of the mixed-layer specific humidity q over the region in which the zonal gradient occurs, specifically from 72.8°E to 73.4°E. Δx represents changes over spatial scales of about 70 km and time-scales of 2 hr for 10 m/s flow. LHF is the moistening due to surface latent heat fluxes, h is the depth of the mixed layer, w_e is the mixing rate between the mixed layer and the drier air above it (in m/s), $\Delta q/\Delta z|_{top}$ is the vertical jump in moisture across the top of the mixed layer, and P_{evap} is moistening from evaporation of precipitation into the mixed layer. Variables u, v, x, y, and t have their usual meanings.

We can use aircraft and satellite measurements to estimate some terms in Equation 1. We cannot estimate the first (moisture tendency), third (meridional advection, because the flights were in the zonal direction) and the last (rainfall evaporation). We also cannot estimate the mixed-layer-top entrainment velocity w_e. Because the boundary-layer zonal moisture gradient occurred on all flights, we focus on two in particular in which these unmeasurable terms are arguably small: B964 (red) and B965 (magenta). These flights occurred on the same day, 26 June, with low-level runs at approximately 1215 and 1845 local time, respectively. The local change in q between these two flights ($\Delta q/\Delta t$) was much smaller than the zonal gradient in q. We do not know the meridional advection, but east of 72.7°E, v was much smaller than u on both flights, and we generally expect that meridional moisture gradients are weaker than zonal gradients in this region. There was also almost no precipitation (measured by IMERG) during these flights. For these two flights, we suggest that the first, third, and last terms in Equation 1 can be eliminated, and the equation re-arranged as:

$$w_e = \frac{1}{\Delta q/\Delta z|_{top}}\left(\frac{LHF}{h} - u\frac{\Delta q}{\Delta x}\right). \quad (2)$$

The right-hand side of Equation 2 can be estimated from aircraft and satellite observations, while w_e, the unknown, represents the entrainment rate between the mixed layer and the drier air above that is required to maintain the observed zonal moisture gradient in the face of moistening by latent heat fluxes and zonal advection. The mixed-layer depth h and vertical moisture jump over the top of the mixed layer $\Delta q/\Delta z|_{top}$ were estimated from the upwind aircraft profile (Figure 12). Latent heat fluxes were calculated using the eddy covariance method from aircraft observations as in Cook and Renfrew (2014). Because the WVSSII humidity observations are only available at 1 Hz, we used the dew point temperature measured by the uncalibrated General Eastern thermoelectric hygrometer, available at 4 Hz. Figure 13 compares the humidity and estimated latent heat flux observations for the two instruments on both flights. Vertical velocity combined from the GIN and turbulence probe was subsampled

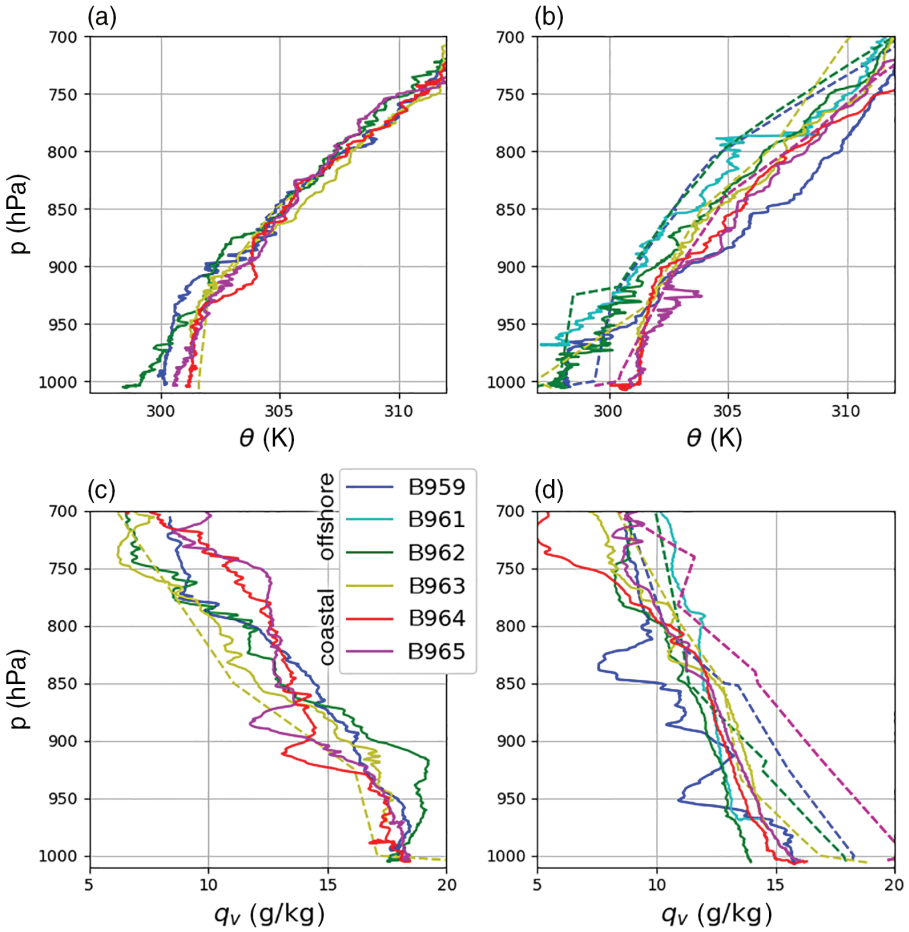

FIGURE 12 Boundary-layer profiles of (a, b) potential temperature (K) and (c, d) specific humidity (g/kg) over the Arabian Sea from aircraft ascent/descent (solid lines) and associated radiosonde launches (dashed lines). (a, c) show aircraft profiles between 72 and 73°E and radiosonde launches from Amini Island. (b, d) show aircraft profiles between 73 and 74°E and radiosonde launches from Mangaluru (Figure 2a shows locations). Only radiosonde launches within 6 hr of the respective aircraft profile (same colour) are shown; note that Amini Island radiosonde launches are at 0000 UTC only. B959–B962 (blue, cyan, green) are during the offshore phase; B963–B965 (yellow, red, magenta) are during the coastal phase

from 32 to 4 Hz to calculate eddy covariances, with averages taken for 2 min (covering about 12 km, roughly ten large eddy length-scales). Zonal moisture advection was estimated entirely from the aircraft observations of u and q on the low-level run. Zonal gradients were calculated as differences between the western and eastern edges of the box from 72.8 to 73.4°E, vertical gradients were calculated as differences between the top and bottom of the mixed layers as estimated by eye from the upwind aircraft profiles, and the LHF was averaged over the length of the run from 72.8 to 73.4°E.

Table 4 shows each term in Equation 2 for flights B964 and B965. The moistening by surface latent heat fluxes was much less than that by zonal advection. It is plausible that latent heat fluxes were higher upwind (beyond the range of the aircraft) and that a decrease in LHF contributed to the drop in humidity. However, climatological estimates of latent heat fluxes over the Arabian Sea do not suggest that this should be the case (Figure 13). Both ERA-Interim and the Goddard Satellite-based Surface Turbulent Fluxes (GSSTF) climatology show a decrease in surface latent heat flux by 20–30 W/m^2 from the open ocean (about 69°E) to the near-offshore region where the boundary layer drying was observed. For a 500 m deep mixed layer (a lower estimate), this decrease in surface latent heat flux would reduce mixed-layer moistening by about 0.07 g/kg per hour. This LHF drop is insufficient to explain the 2–4 g/kg drop in moisture over comparable time-scales shown in Figure 11. Therefore, although our LHF calculations are problematic in that they are based on an uncalibrated instrument, independent estimates of LHF strongly suggest that gradients in LHF do not explain the drop in q as the flow approaches the coast.

The fourth column in Table 4 shows that there is a moderately large drop in moisture above the top of the mixed layer (Figure 12c). The fifth column shows the mixed-layer vertical entrainment rate w_e required to maintain the observed zonal gradient in moisture against latent heat fluxes and zonal advection (i.e. calculated from Equation 2). The estimated values of w_e are 5–7 cm/s. Bhat and Fernando (2016) observed similar entrainment rates over the Arabian Sea in conditions of high shear; in our observations, increases in zonal wind speed of about 10 m/s over the lowest kilometre were measured in the westernmost aircraft profiles of B964 and B965 (not shown). Furthermore, what we are calling entrainment here really represents any process that mixes free

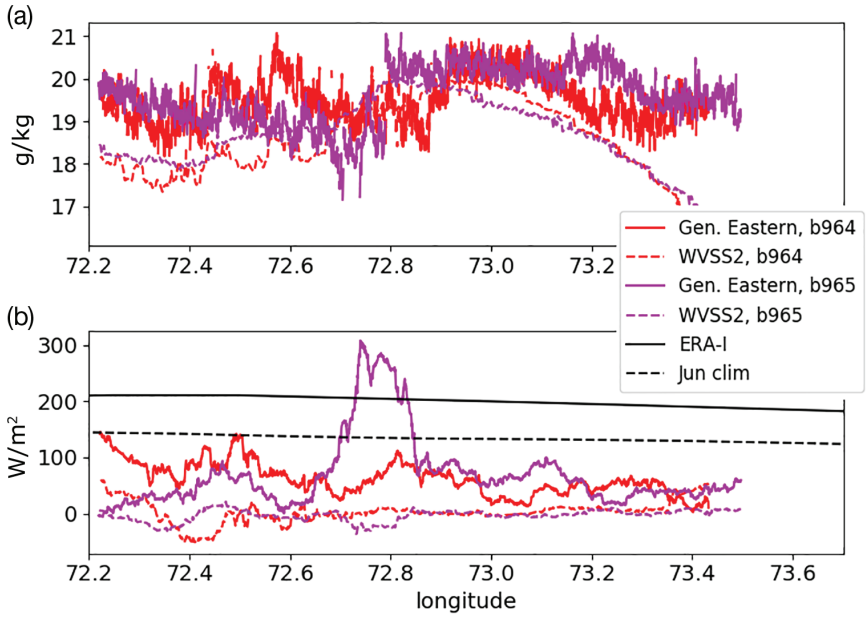

FIGURE 13 (a) Specific humidity (g/kg) and (b) estimates of surface latent heat flux (W/m^2) from low-level runs over the Arabian Sea (colours), ERA-Interim on 26 June, 0000–1200 UTC mean (solid black, 0530 to 1730 local time), and Goddard Satellite-based Surface Turbulent Fluxes (GSSTF, dashed black) climatology for June 1998–2008

TABLE 4 Terms in Equation 2. Δq represents the jump in humidity across the top of the mixed layer in the upwind aircraft profile, normalized per 100 m. The boundary-layer depth h was estimated from the upwind aircraft potential temperature profiles (Figure 12a)

Flight	LHF (g kg^{-1} hr^{-1})	$-u\Delta q/\Delta x$ (g kg^{-1} hr^{-1})	Δq (g/kg per 100 m)	w_e (cm/s)	h (m)
B964	0.05	1.37	−0.82	4.8	1100
B965	0.08	1.40	−0.63	6.5	800

tropospheric air into the mixed layer, including ventilation from downdraughts, mixing by boundary-layer eddies, and entrainment between the top of the subcloud mixed layer and the cloud layer. The large spatial and day-to-day variability in mixed-layer temperature and winds during the offshore phase (Figure 11) is further evidence that convective downdraughts were active during that time. This mixing of free tropospheric air into the subcloud mixed layer can account for the observed drop in humidity as the flow approaches the coast, while other processes, such as changes in latent heat fluxes, likely cannot.

Figure 12 shows that the drop in humidity near the coast is mostly confined to the lower boundary layer, usually below 900 hPa. The notable exception is flight B959, which is also the flight during which the most rain fell (Figure 11). In the eastern Arabian Sea profile on B959, several dry layers below 800 hPa were evident. These dry layers coincided with increased stability in the potential temperature profiles, suggesting that convective downdraughts mixed dry, potentially warmer air into the boundary layer as a significant part of the boundary-layer drying seen in Figure 12. These layers were not necessarily vertically stacked, as the aircraft flew about 20 km horizontally for every 1,000 m of elevation change.

Zonal structures in addition to those above are seen by comparing the left and right profiles in Figure 12. A much greater range in potential temperature occurred closer to the coast than upstream, particularly during the offshore phase. The moisture measurements in the radiosonde data – to the extent that it is not subject to the errors due to slow humidity sensors discussed above – suggest that the onshore flow humidity increased again before or when it hit the coast.

We have shown that there was considerable variability in Arabian Sea boundary-layer temperature, humidity, and winds over the course of the IOP. This variability was generally much higher during the offshore phase, suggesting that this variability is tied to convection. However, even in the absence of convection, a persistent drying of the boundary layer was seen throughout the aircraft observations, likely due to mixing with the free troposphere. Furthermore, there was far less variability in temperature and humidity west of about 72.5°E. This suggests that, over the remote ocean, a balance of processes kept variations in temperature and moisture relatively small, but that this balance was disrupted as the flow approached the coast.

6 | PRECIPITATION RESPONSE OVER LAND

Thus far our detailed analysis has focused on aircraft observations over the Arabian Sea. The flux tower site at Dharwad

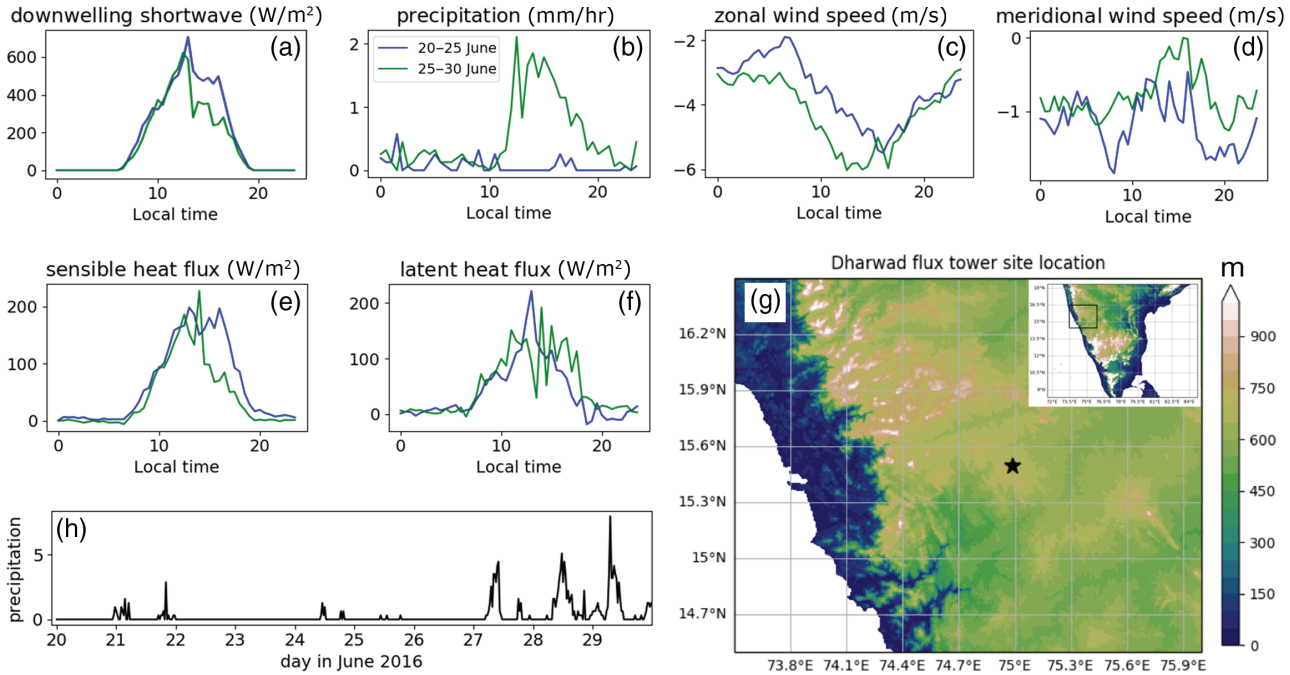

FIGURE 14 (a–f) Diurnal cycle of tower data and IMERG precipitation at Dharwad. Blue lines represent the first 5 days of the IOP (the offshore phase) and green lines represent the last 5 days (the coastal phase). (h) shows time series of IMERG rainfall (mm/hr) at Dharwad and (g) the location of the Dharwad site with local elevation (m)

on the lee slopes of the Western Ghats allows us also to study the surface processes in the mountains during the IOP. Forthcoming work will provide a more comprehensive overview of flux tower measurements from this site and others associated with INCOMPASS.

Figure 14 shows the diurnal cycles of short-wave radiation, precipitation, winds, and latent and sensible heat fluxes from the Dharwad flux tower site, whose location is also shown in Figure 14. Because of errors in the precipitation measurements at the flux tower site during this period, we used IMERG rainfall from the gridpoint nearest to the Dharwad location.

The offshore phase had weak rainfall with no diurnal signal, while the coastal phase had a clear diurnal cycle, with almost all rain falling in the afternoon and evening, as also seen in the modelling study of Flynn *et al.* (2017). Both phases had a fairly strong diurnal cycle in zonal wind, with weak easterlies at night and morning becoming stronger in the afternoon. These easterlies were embedded within large-scale westerly flow; we thus expect them to be associated with low-level convergence. The magnitude of the peak in the easterlies was greater in the coastal phase and also occurred earlier in the afternoon, several hours before the peak during the offshore phase. Meridional winds were weak and had little diurnal cycle in either phase, although they were weakest in the afternoon. Examination of the orography around the Dharwad site (Figure 14g) suggests that winds at this time were dominated by upslope flow from the valley east by northeast of the site. This upslope flow increased during the day, possibly in response to diurnal heating, and converged with the onshore flow. In the diurnal mean, the enhanced upslope flow began several hours before rainfall started, suggesting that it triggered precipitation rather than only responding to it.

Latent heat fluxes had similar magnitudes and diurnal cycles in both phases. Wetting of the path measured by the flux tower's infrared gas analyser during heavy rainfall prevents accurate latent heat flux measurements, so the data in the coastal phase has many gaps. The sensible heat flux and solar radiation were similar in both phases in the morning, but afternoon cloud shading and surface wetting reduced both of these during the coastal phase. The partition of energy between sensible and latent heat flux at Darwad strongly contrasted between the two periods, with mean evaporative fraction (average from 1000 to 1400 local time) rising from 0.49 in the offshore phase to 0.76 in the coastal phase. At this time of year, when soils are still dry, the surface energy balance is very sensitive to rainfall.

Both local surface heating and changes in the synoptic-scale flow combined to produce the observed diurnal cycle in rainfall at Dharwad within the Western Ghats during the IOP. Figures 7 and 11 show that the low-level onshore flow was stronger during the coastal phase than during the offshore phase, and Figure 11 also suggests that the lowest few hundred metres (the source of convective air parcels) had higher specific humidity in the coastal phase because there was less deep convection offshore to ventilate the boundary layer. Additionally, the earlier and stronger peak in upslope easterlies (Figure 14) may have enhanced convective triggering over the mountains during the coastal phase. This change in the upslope flow might have been a mesoscale response to the synoptic evolution, including possibly enhanced solar heating in the valley east of Dharwad,

as observers on the ground in Bengaluru noted that the sky was clearer during the coastal phase than during the offshore phase.

7 | SUMMARY AND CONCLUSION

The southern phase of the INCOMPASS field campaign took place from 21 to 27 June 2016 and included six flights from the base in Bengaluru to the west, over the Western Ghats coastal mountain range and eastern Arabian Sea, a region with some of the heaviest precipitation associated with the South Asian monsoon. These flights sampled the diurnal cycle and the passage of a large-scale band of heavy rainfall over the Arabian Sea.

In this paper we used aircraft observations as well as those from a new INCOMPASS flux tower in the Western Ghats, along with satellite observations and reanalysis to guide interpretation, to address the following questions.

How did the synoptic evolution affect the spatial pattern of rainfall over the mountains and offshore?
What physical parameters were most associated with the change in rainfall offshore?
What was the boundary-layer structure offshore, and how did that structure change as the flow approached the coast and in association with the changing synoptic conditions?
How did convection and circulation over the Western Ghats change?

Over the course of the field campaign over South India, the rainfall regime shifted from one of widespread rainfall over both the southeastern Arabian Sea and the southwestern Bay of Bengal, to heavy rainfall over the Western Ghats. This shift was governed by the northward propagation of the Bay of Bengal monsoon low pressure system and the adjacent band of precipitation over the Arabian Sea, which itself intensified into a low pressure system in the north Arabian Sea. This northward propagating band of rainfall represented the passage of an active phase of the Boreal Summer Intraseasonal Oscillation. While the precipitating systems propagated northward in both seas, an incursion of mid-level dry air from the western Arabian Sea suppressed convection over the Arabian Sea and, to a lesser extent, South India. Enhanced onshore flow over the Western Ghats produced local convection there. Diurnal cycles similar to the modelling study of Flynn *et al.* (2017) were seen: during the offshore phase rainfall peaked offshore in the morning; during the coastal phase rainfall peaked on the mountains in the afternoon.

The schematic diagrams in Figure 15 summarize the important differences between the two regimes sampled in this project in the region of the eastern Arabian Sea and Western Ghats mountains.

During the offshore phase (Figure 15a; 21–24 June), relatively weak onshore flow, a cool, relatively dry boundary layer, a low critical layer (height where $u = 0$) with a positive potential temperature anomaly above it, and moist mid-troposphere were associated with closely spaced convective clouds with tops rarely higher than 400 hPa several hundred kilometres offshore. Houze *et al.* (2015) noted that this arrangement of closely spaced moderate convective clouds is a common feature upstream of the Western Ghats during the monsoon as seen by the TRMM Precipitation Radar. The offshore convective clouds produced heavy showers and many detraining layers of altocumulus and altostratus, as noted by mission scientists. Widespread cirrus clouds between about 300 and 100 hPa were also observed offshore by infrared satellite and observers on the aircraft. The injection of free tropospheric air into the boundary layer via both downdraughts and boundary-layer entrainment reduced humidity in the lowest layers of the onshore flow as it approached the coast, raising the cloud base.

Nearer to the coast, the moderate convective clouds matured into stratiform, and a stratiform cloud mass produced rain on the upstream side of the Western Ghats. The critical height tilted down to the east over the Western Ghats and a warm potential temperature anomaly was observed just above the critical height; both of these features are consistent with numerical solutions of stable flow over a Gaussian ridge. During the offshore phase, stratiform rain fell on the Western Ghats, but at lower rates than the climatology for late June. An easterly upslope flow occurred in the afternoon in some locations on the lee slopes of the mountains, but this upslope flow did not trigger convection.

During the coastal phase (Figure 15b; 25–28 June), the onshore westerlies were stronger and deeper, with a higher critical layer. A mid-tropospheric dry intrusion originating from the western Arabian Sea suppressed deep convection offshore, allowing moisture to accumulate in the lowest levels of the boundary layer to as much as 20 g/kg, the highest values observed during the IOP. The dry intrusion dipped downward to the east, increasing the efficiency of entrainment drying of the boundary layer as the flow approached the coast. The onshore flow was both stronger and, in the lowest layers, more moist than during the offshore phase, despite the entrainment drying. Additionally, the diurnally driven upslope easterly flow on the lee side of the mountains was stronger and occurred earlier in the day than during the offshore phase. This stronger, earlier upslope flow combined with stronger, more moist onshore flow to enhance convection over the tops of the Western Ghats, including at the Dharwad site just east of the ridge. Rainfall on the upstream side of the Western Ghats was also heavier during the mountain phase than the offshore phase.

These results suggest the following.

1. Orographic blocking may contribute to offshore rainfall, but local thermodynamic properties such as SST and mid-tropospheric humidity play a more significant role. This result is consistent with the numerical modelling results of Ogura and Yoshizaki (1988) and Zhang and Smith (2018).

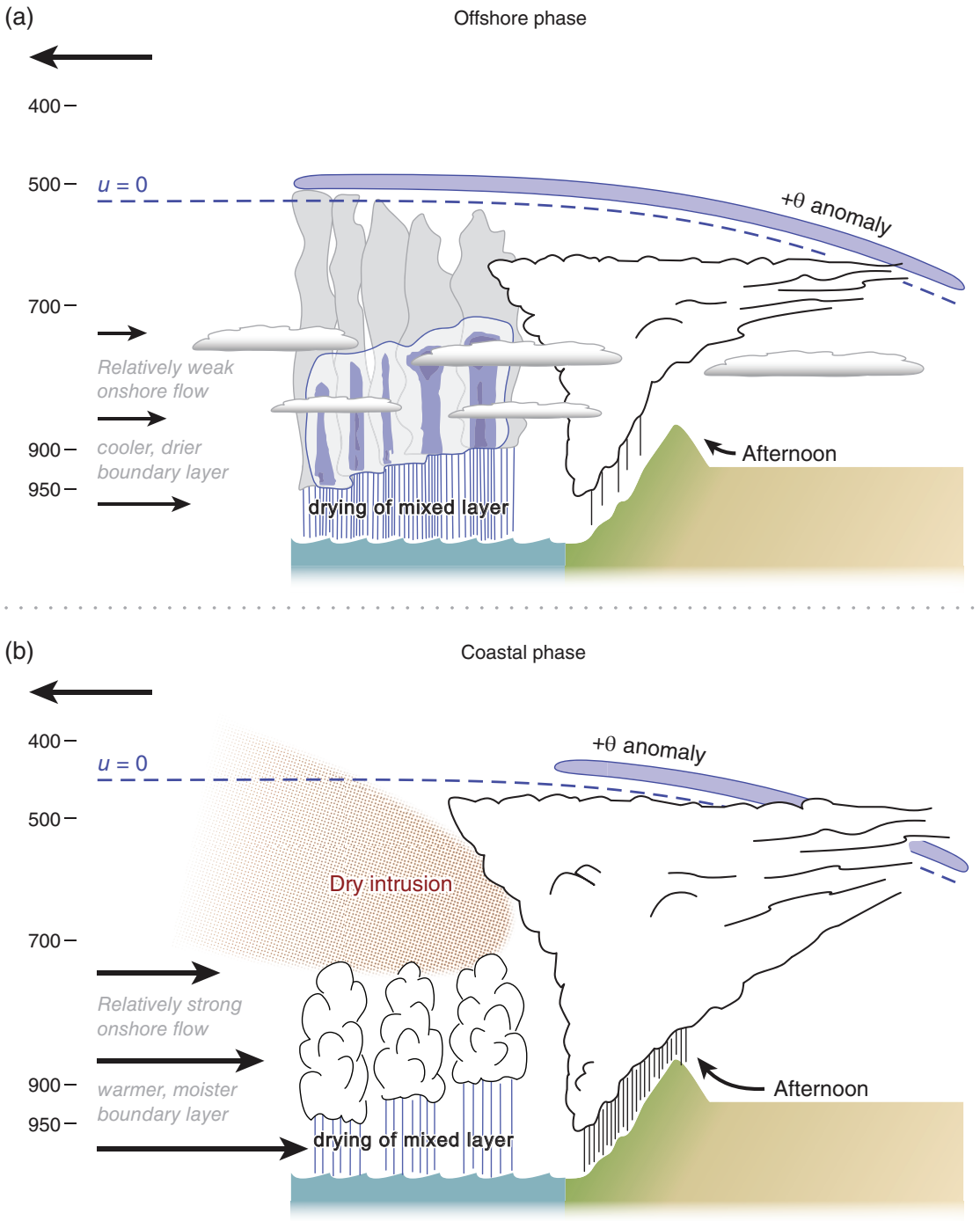

FIGURE 15 Schematic of the most important features of (a) the offshore phase and (b) the coastal phase. Section 7 gives discussion. Art by Beth Tully

2. Mid-tropospheric dry intrusions have a profound impact on the magnitude of rainfall offshore and on the thermodynamics of the low-level onshore flow. By suppressing convection offshore, they allow build-up of boundary-layer humidity as the flow approaches the coast, possibly enhancing rainfall over the Western Ghats. Similar re-charging of boundary-layer moisture under a dry intrusion was observed during the TOGA-COARE experiment (Tropical Ocean Global Atmospheres/Coupled Ocean–Atmosphere Response Experiment; Parsons *et al.*, 2000). This mechanism would produce the trade-off in rainfall offshore and over land suggested by Zhang and Smith (2018) and observed in this campaign.

3. Upslope flow from the Deccan Plateau to the peaks of the Western Ghats occurs regularly in the afternoons, and can help trigger rainfall on the eastern slopes of the mountains if other conditions (e.g. the strength and moisture content of the onshore flow) support it.

The observations presented in this paper provide a useful framework for detailed climatological studies and modelling experiments, which we can use to test hypotheses with greater rigour. We have recently carried out a 4.4 km resolution

simulation of the 2016 monsoon season for all of South Asia and will present analysis of this simulation in future studies. In this and higher-resolution simulations, we can address the following questions, among others:

- Are shifts between offshore and coastal rainfall in this region observed climatologically? If so, what synoptic regimes are associated with these shifts, and are they reproduced in models? What role does the variable depth and intensity of convection play in the overall character of the offshore versus coastal phases?
- How much of offshore rainfall is locally generated and how much propagates downshear from convection initiated over the Western Ghats? What role does the strength and depth of the Somali jet play in determining whether rainfall over the mountains propagates offshore?
- What mesoscale circulation changes occur over the Western Ghats in response to changes in the strength and humidity of the onshore flow?
- Can a high-resolution model reproduce the observed variability of the low-level onshore flow? This variability includes low-level zonal wind speeds varying from 0 to 25 m/s in convective environments as well as persistent boundary-layer drying of 4 g/kg over 100 km over a wide range of convective regimes. If so, what mechanisms produced this drying, and why did it always occur east of 72°E?

Addressing these and other questions informed by these observations may guide improvements in predicting the timing and spatial distribution of rainfall over South India during the monsoon. If the synoptic conditions associated with specific types of convection are better known, forecasters can use that information in their warnings and advisories. If the interaction of these types of convection with the large-scale flow and surface are better understood, improvements in their representation in climate models may reduce model biases for India and improve confidence in intra-seasonal and longer time-scale predictions.

ACKNOWLEDGEMENTS

This work was supported by Natural Environment Research Council grants NE/L013843/1, NE/L01386X/1, and NE/L013819/1. D. J. Parker is also supported by a Royal Society Wolfson Research Merit Award. The Indian part of the INCOMPASS project is funded by the Ministry of Earth Sciences through its Monsoon Mission Program and implemented through the Indian Institute of Tropical Meteorology, Pune. G.M. Martin was supported by the Joint UK BEIS/Defra Met Office Hadley Centre Climate Programme (GA01101). S. R. Brodzik is supported by National Science Foundation grant AGS-1503155 and National Aeronautics and Space Administration grant NNX16AD75G. R. A. Houze is supported by National Science Foundation grant AGS-1503155, National Aeronautics and Space Administration grant NNX16AD75G, and the Pacific Northwest National Laboratory under task order 292896 (WACCEM) of master agreement 243766. We thank Dr. Ross Morrison for assistance using flux tower data, the India Meteorology Department for station radiosonde data, and Beth Tully for graphics.

ORCID

Jennifer K. Fletcher https://orcid.org/0000-0002-4892-3344
Douglas J. Parker https://orcid.org/0000-0003-2335-8198
Andrew G. Turner https://orcid.org/0000-0002-0642-6876
Kieran M. R. Hunt https://orcid.org/0000-0003-1480-3755
Christopher M. Taylor https://orcid.org/0000-0002-0120-3198

REFERENCES

Annamalai, H. and Slingo, J. (2001) Active/break cycles: diagnosis of the intraseasonal variability of the Asian summer monsoon. *Climate Dynamics*, 18(1–2), 85–102.

Annamalai, H. and Sperber, K. (2005) Regional heat sources and the active and break phases of boreal summer intraseasonal (30–50 day) variability. *Journal of the Atmospheric Sciences*, 62(8), 2726–2748.

Bhat, G.S. and Fernando, H.J. (2016) Remotely driven anomalous sea–air heat flux: over the north Indian Ocean during the summer monsoon season. *Oceanography*, 29(2), 232–241.

Bhat, G.S. and Narasimha, R. (2007) Indian summer monsoon experiments. *Current Science*, 93(2), 153–164.

Bhat, G., Vecchi, G. and Gadgil, S. (2004) Sea surface temperature of the Bay of Bengal derived from the TRMM microwave imager. *Journal of Atmospheric and Oceanic Technology*, 21(8), 1283–1290.

Cook, P.A. and Renfrew, I.A. (2014) Aircraft-based observations of airsea turbulent fluxes around the British Isles. *Quarterly Journal of the Royal Meteorological Society*, 141, 139–152. https://doi.org/10.1002/qj.2345.

Dee, D.P., Uppala, S., Simmons, A., Berrisford, P., Poli, P., Kobayashi, S., Andrae, U., Balmaseda, M., Balsamo, G., Bauer, P., Bechtold, P., Beljaars, A.C.M., van de Berg, L., Bidlot, J., Bormann, N., Delsol, C., Dragani, R., Fuentes, M., Geer, A.J., Haimberger, L., Healy, S.B., Hersbach, H., Hólm, E.V., Isaksen, L., Kållberg, P., Köhler, M., Matricardi, M., McNally, A.P., Monge-Sanz, B.M., Morcrette, J.-J., Park, B.-K., Peubey, C., de Rosnay, P., Tavolato, C., Thépaut, J.-N. and Vitart, F. (2011) The ERA-Interim reanalysis: configuration and performance of the data assimilation system. *Quarterly Journal of the Royal Meteorological Society*, 137, 553–597.

Findlater, J. (1969) A major low-level air current near the Indian Ocean during the northern summer. *Quarterly Journal of the Royal Meteorological Society*, 95, 362–380.

Flynn, W.J., Nesbitt, S.W., Anders, A.M. and Garg, P. (2017) Mesoscale precipitation characteristics near the Western Ghats during the Indian Summer Monsoon as simulated by a high-resolution regional model. *Quarterly Journal of the Royal Meteorological Society*, 143, 3070–3084.

Francis, P. and Gadgil, S. (2006) Intense rainfall events over the west coast of India. *Meteorology and Atmospheric Physics*, 94(1), 27–42.

Gadgil, S. (1977) Orographic effects on the southwest monsoon: a review. *Pure and Applied Geophysics*, 115(5–6), 1413–1430.

Grossman, R.L. and Durran, D.R. (1984) Interaction of low-level flow with the Western Ghat mountains and offshore convection in the summer monsoon. *Monthly Weather Review*, 112(4), 652–672.

Hirose, M. and Nakamura, K. (2005) Spatial and diurnal variation of precipitation systems over Asia observed by the TRMM Precipitation Radar. *Journal of Geophysical Research*, 110. https://doi.org/10.1029/2004JD004815.D05106.

Houze, R.A. (1997) Stratiform precipitation in regions of convection: a meteorological paradox? *Bulletin of the American Meteorological Society*, 78(10), 2179–2196.

Houze, R.A. (2014) *Cloud Dynamics*. Cambridge, MA: Academic Press.

Houze, R.A., Rasmussen, K.L., Zuluaga, M.D. and Brodzik, S.R. (2015) The variable nature of convection in the tropics and subtropics: a legacy of 16 years of the Tropical Rainfall Measuring Mission satellite. *Reviews of Geophysics*, 53(3), 994–1021.

Huffman, G.J., Bolvin, D.T., Nelkin, E.J., Wolff, D.B., Adler, R.F., Gu, G., Hong, Y., Bowman, K.P. and Stocker, E.F. (2007) The TRMM multisatellite precipitation analysis (TMPA): Quasi-global, multiyear, combined-sensor precipitation estimates at fine scales. *Journal of Hydrometeorology*, 8(1), 38–55.

Kikuchi, K., Wang, B. and Kajikawa, Y. (2012) Bimodal representation of the tropical intraseasonal oscillation. *Climate Dynamics*, 38(9–10), 1989–2000.

Klemp, J.B. and Lilly, D.K. (1978) Numerical simulation of hydrostatic mountain waves. *Journal of the Atmospheric Sciences*, 35(1), 78–107.

Konwar, M., Das, S., Deshpande, S., Chakravarty, K. and Goswami, B. (2014) Microphysics of clouds and rain over the Western Ghat. *Journal of Geophysical Research*, 119(10), 6140–6159.

Krishnamurti, T. (1985) Summer monsoon experiment – a review. *Monthly Weather Review*, 113(9), 1590–1626.

Kulkarni, J.R., Maheskumar, R.S., Morwal, S.B., Padma Kumari, B., Konwar, M., Deshpande, C.G., Joshi, R.R., Bhalwankar, R.V., Pandithurai, G., Safai, P.D., Narkhedkar, S.G., Dani, K.K., Nath, A., Nair, S., Sapre, V.V., Puranik, P.V., Kandalgaonkar, S.S., Mujumdar, V.R., Khaladkar, R.M., Vijayakumar, R., Prabha, T.V. and Goswami, B.N. (2012) The cloud aerosol interactions and precipitation enhancement experiment (CAIPEEX): overview and preliminary results. *Current Science*, 102(3), 413–425.

Kumar, S. and Bhat, G.S. (2017) Vertical structure of orographic precipitating clouds observed over south Asia during summer monsoon season. *Journal of Earth System Science*, 126(8), 114.

Levine, R.C. and Turner, A.G. (2012) Dependence of Indian monsoon rainfall on moisture fluxes across the Arabian Sea and the impact of coupled model sea surface temperature biases. *Climate Dynamics*, 38(11–12), 2167–2190.

Levine, R.C., Turner, A.G., Marathayil, D. and Martin, G.M. (2013) The role of northern Arabian Sea surface temperature biases in CMIP5 model simulations and future projections of Indian summer monsoon rainfall. *Climate Dynamics*, 41(1), 155–172.

Liebmann, B. and Smith, C.A. (1996) Description of a complete (interpolated) outgoing longwave radiation dataset. *Bulletin of the American Meteorological Society*, 77(6), 1275–1277.

Lin, X. and Johnson, R.H. (1996) Kinematic and thermodynamic characteristics of the flow over the western Pacific warm pool during TOGA COARE. *Journal of the Atmospheric Sciences*, 53(5), 695–715.

Maheskumar, R., Narkhedkar, S., Morwal, S., Padmakumari, B., Kothawale, D., Joshi, R., Deshpande, C., Bhalwankar, R. and Kulkarni, J. (2014) Mechanism of high rainfall over the Indian west coast region during the monsoon season. *Climate Dynamics*, 43(5–6), 1513–1529.

Mapes, B.E. and Houze, R.A. (1992) An integrated view of the 1987 Australian monsoon and its mesoscale convective systems. I: horizontal structure. *Quarterly Journal of the Royal Meteorological Society*, 118, 927–963.

Mapes, B.E. and Zuidema, P. (1996) Radiative-dynamical consequences of dry tongues in the tropical troposphere. *Journal of the Atmospheric Sciences*, 53(4), 620–638.

McCreary, J.P. and Kundu, P.K. (1989) A numerical investigation of sea surface temperature variability in the Arabian Sea. *Journal of Geophysical Research*, 94(C11), 16097–16114.

Mitra, A.K., Momin, I., Rajagopal, E., Basu, S., Rajeevan, M. and Krishnamurti, T. (2013) Gridded daily Indian monsoon rainfall for 14 seasons: merged TRMM and IMD gauge analyzed values. *Journal of Earth System Science*, 122(5), 1173–1182.

Ogura, Y. and Yoshizaki, M. (1988) Numerical study of orographic-convective precipitation over the eastern Arabian Sea and the Ghat Mountains during the summer monsoon. *Journal of the Atmospheric Sciences*, 45(15), 2097–2122.

Parsons, D.B., Redelsperger, J.L. and Yoneyama, K. (2000) The evolution of the tropical western Pacific atmosphere-ocean system following the arrival of a dry intrusion. *Quarterly Journal of the Royal Meteorological Society*, 126, 517–548.

Rajeevan, M., Gadgil, S. and Bhate, J. (2010) Active and break spells of the Indian summer monsoon. *Journal of Earth System Science*, 119(3), 229–247.

Rao, P.S. (2005) Arabian Sea monsoon experiment: an overview. *Mausam*, 56(1), 1–7.

Rao, Y.P. (1976) *Southwest Monsoon*. Synoptic meteorology monograph N.1/1976. Pune: India Meteorological Department.

Reynolds, R.W., Smith, T.M., Liu, C., Chelton, D.B., Casey, K.S. and Schlax, M.G. (2007) Daily high-resolution-blended analyses for sea surface temperature. *Journal of Climate*, 20(22), 5473–5496.

Romatschke, U. and Houze, R.A. (2011) Characteristics of precipitating convective systems in the South Asian monsoon. *Journal of Hydrometeorology*, 12(1), 3–26.

Romatschke, U., Medina, S. and Houze, R.A. (2010) Regional, seasonal, and diurnal variations of extreme convection in the South Asian region. *Journal of Climate*, 23(2), 419–439.

Roundy, P.E. (2012) Tracking and prediction of large-scale organized tropical convection by spectrally focused two-step space–time EOF analysis. *Quarterly Journal of the Royal Meteorological Society*, 138, 919–931.

Saha, K. (1970) Zonal anomaly of sea surface temperature in equatorial Indian Ocean and its possible effect upon monsoon circulation. *Tellus*, 22(4), 403–409.

Saha, S.K., Pokhrel, S., Chaudhari, H.S., Dhakate, A., Shewale, S., Sabeerali, C., Salunke, K., Hazra, A., Mahapatra, S. and Rao, A.S. (2014) Improved simulation of Indian summer monsoon in latest NCEP climate forecast system free run. *International Journal of Climatology*, 34(5), 1628–1641.

Sathiyamoorthy, V., Mahesh, C., Gopalan, K., Prakash, S., Shukla, B.P. and Mathur, A.K. (2013) Characteristics of low clouds over the Arabian Sea. *Journal of Geophysical Research*, 118(24), 13489–13503.

Shie, C.L., Adler, R., Lin, I.-I., Nelkin, E., Ardizzone, J. and Gao, S. (2012) *Goddard Satellite-Based Surface Turbulent Fluxes, 0.25 x 0.25 deg, Daily Grid*. Technical report. GESDISC, Greenbelt, MD. Available at: https://disc.gsfc.nasa.gov/datasets/GSSTF_F08_V3 [Accessed 4th January 2019]

Shige, S., Nakano, Y. and Yamamoto, M.K. (2017) Role of orography, diurnal cycle, and intraseasonal oscillation in summer monsoon rainfall over the Western Ghats and Myanmar Coast. *Journal of Climate*, 30(23), 9365–9381.

Shrestha, D., Deshar, R. and Nakamura, K. (2015) Characteristics of summer precipitation around the Western Ghats and the Myanmar West Coast. *International Journal of Atmospheric Sciences*, 2015. https://doi.org/10.1155/2015/206016.

Shukla, J. (1975) Effect of Arabian sea-surface temperature anomaly on Indian summer monsoon: a numerical experiment with the GFDL model. *Journal of the Atmospheric Sciences*, 32(3), 503–511.

Sikka, D. (2005) From the International Indian Ocean Experiment (IIOE) to the Arabian Sea Monsoon Experiment (ARMEX) – four decades of major advances in monsoon meteorology. *Mausam*, 56(1), 19–36.

Smith, R.B. (1985) Comment on Interaction of low-level flow with the Western Ghat Mountains and offshore convection in the summer monsoon. *Monthly Weather Review*, 113(12), 2176–2177.

Smolarkiewicz, P.K. and Rotunno, R. (1989) Low Froude number flow past three-dimensional obstacles. Part I: baroclinically generated lee vortices. *Journal of the Atmospheric Sciences*, 46(8), 1154–1164.

Sperber, K.R., Annamalai, H., Kang, I.S., Kitoh, A., Moise, A., Turner, A., Wang, B. and Zhou, T. (2013) The Asian summer monsoon: an intercomparison of CMIP5 versus CMIP3 simulations of the late 20th century. *Climate Dynamics*, 41(9-10), 2711–2744.

Stevens, B. (2006) Bulk boundary-layer concepts for simplified models of tropical dynamics. *Theoretical and Computational Fluid Dynamics*, 20(5), 279–304.

Thompson, R.M., Payne, S.W., Recker, E.E. and Reed, R.J. (1979) Structure and properties of synoptic-scale wave disturbances in the intertropical convergence zone of the eastern Atlantic. *Journal of the Atmospheric Sciences*, 36(1), 53–72.

Utsav, B., Deshpande, S.M., Das, S.K. and Pandithurai, G. (2017) Statistical characteristics of convective clouds over the Western Ghats derived from weather radar observations. *Journal of Geophysical Research*, 122(18), 10050–10076.

Vance, A., Abel, S., Cotton, R. and Woolley, A. (2015) Performance of WVSS-II hygrometers on the FAAM research aircraft. *Atmospheric Measurement Techniques*, 8(3), 1617–1625.

Virts, K.S. and Houze, R.A. (2016) Seasonal and intraseasonal variability of mesoscale convective systems over the South Asian monsoon region. *Journal of the Atmospheric Sciences*, 73(12), 4753–4774.

Walters, D., Brooks, M., Boutle, I., Melvin, T., Stratton R, Vosper, S.B., Wells, H., Williams, K., Wood, N., Allen, T., Bushell, A., Copsey, D., Earnshaw, P., Edwards, J., Gross, M., Hardiman, S., Harris, C., Heming, J., Klingaman, N., Levine, R., Manners, J., Martin, G., Milton, S., Mittermaier, M., Morcrette, C., Riddick, T., Roberts, M., Sanchez, C., Selwood, P., Stirling, A., Smith, C., Suri, D., Tennant, W., Vidale, P.L., Wilkinson, J., Willett, M., Woolnough, S. and Xavier, P. (2017) The Met Office Unified Model Global Atmosphere 6.0/6.1 and JULES Global Land 6.0/6.1 configurations. *Geoscientific Model Development*, 10(4), 1487–1520. https://doi.org/10.5194/gmd-10-1487-2017.

Ward, H., Evans, J.G. and Grimmond, C.S.B. (2013) Multi-season eddy covariance observations of energy, water and carbon fluxes over a suburban area in Swindon, UK. *Atmospheric Chemistry and Physics*, 13(9), 4645–4666.

Wheeler, M.C. and Hendon, H.H. (2004) An all-season real-time multivariate MJO index: development of an index for monitoring and prediction. *Monthly Weather Review*, 132(8), 1917–1932.

Willetts, P., Marsham, J., Birch, C.E., Parker, D.J., Webster, S. and Petch, J. (2017) Moist convection and its upscale effects in simulations of the Indian monsoon with explicit and parametrized convection. *Quarterly Journal of the Royal Meteorological Society*, 143, 1073–1085.

Zhang, G. and Smith, R.B. (2018) Numerical study of physical processes controlling summer precipitation over the Western Ghats region. *Journal of Climate*, 31, 3099–3115.

How to cite this article: Fletcher JK, Parker DJ, Turner AG, *et al*. The dynamic and thermodynamic structure of the monsoon over southern India: New observations from the INCOMPASS IOP. *Q J R Meteorol Soc*. 2020;146:2867–2890. https://doi.org/10.1002/qj.3439